Available online at www.sciencedirect.com

ScienceDirect

Advances in Space Research 77 (2026) 9105–9126

ADVANCES IN SPACE RESEARCH (a COSPAR publication)

www.elsevier.com/locate/asr

Periodic orbit families around slow-rotating dipole-segment bodies: The case of the asteroid Itokawa

Antonio Elipe [a,*,1], Alessandra F.S. Ferreira [b,2], Alberto Abad [c,1]

[a] Universidad de Zaragoza, Zaragoza, Spain
[b] Universidade Estadual Paulista (UNESP), Brazil
[c] Universidad de Zaragoza, Zaragoza, Spain

Received 24 December 2025; received in revised form 9 February 2026; accepted 10 March 2026
Available online 13 March 2026

Abstract

The Dipole-Segment (DS) model has proven to be a useful approximation for representing the gravitational potential of elongated asteroids with end-point protrusions. The model consists of a massive rod with two spherical masses attached at its extremities, rotating about its center of mass with uniform angular velocity. The potential function depends on three parameters, one of which, κ, is associated with the rotation rate. The dynamical behavior of the system therefore varies significantly between fast- and slow-rotating bodies.

This work provides a comprehensive dynamical characterization of the DS model applied to a slow-rotating asteroid. As a case study, we consider asteroid (25143) Itokawa, for which we compute a complete family map of symmetric periodic orbits and assess their stability properties; these are then compared with analogous families of periodic orbits of the Restricted Three-Body Problem. Furthermore, we identify heteroclinic connections between unstable isosceles equilibria. These results demonstrate that slow rotation gives rise to a significantly richer dynamical structure than previously observed for moderate–to–fast rotations, highlighting the relevance of rotational effects in mission design around small irregular bodies.

Keywords: Orbital dynamics; Families of periodic orbits; Dipole-Segment gravitational field

1. Introduction

The study of asteroids plays a fundamental role in planetary science, as these small bodies retain primordial material that records the early history of the Solar System. Investigating their physical, compositional, and dynamical characteristics provides insights into the processes that shaped the planetary system. Moreover, asteroids represent both potential hazards and valuable resources for future space exploration. In this context, sending orbiters to small, irregularly shaped asteroids has become a key objective of several space missions, enabling direct observation of their surface morphology and internal structure, as well as in situ analysis of their complex gravitational environments. The NEAR Shoemaker mission to the asteroid (433) Eros in 2001 was the first to successfully orbit and land on an asteroid, providing invaluable data on its shape, surface features, and gravity field. Building on that success, the Hayabusa mission to the asteroid (25143) Itokawa further exemplified the challenges of operating around such a small, weakly gravitating body, and it provided high-resolution data that stimulated extensive research on its dynamics and surface processes. Understanding the motion

* Corresponding author.
E-mail address: elipe@unizar.es (A. Elipe).
[1] Instituto Universitario de Matemáticas y Aplicaciones, Spain.
[2] Departamento de Matematica, Brazil.

https://doi.org/10.1016/j.asr.2026.03.036
0273-1177/

of spacecraft and natural particles around this type of bodies therefore remains a topic of considerable scientific and practical interest.

One of the main characteristics of many of these asteroids is its elongated shape, e.g. (1620) Geographos (Ostro et al., 2004), at times with protuberances as it happens with the asteroid (216) Kleopatra, which has a ham-bone shape (Descamps et al., 2011), or (25143) Itokawa (Fig. 1) with shape resembling a "sea otter" composed of a smaller, rather round head and a larger oval body (Fujiwara et al., 2006). For this type irregular shaped bodies, the classical way of expanding the gravitational potential in a Legendre polynomial series is not valid because the convergence radius of the series is bigger than the radius of the sphere that englobes the body, thus, new models to represent the gravitation potential have been proposed in the literature, some models very complete although very costly from the computational point of view, like the use of homogeneous polyhedron (Werner, 1994; Werner and Scheeres, 1997). Other models are simpler and partially sacrifice accuracy in favor of reducing complexity and computation time. Along these lines, there are models whose potential functions can be expressed in closed form, without the need for series expansions. Thus, we have the rotating dipole proposed by Prieto-Llanos and Gómez-Tierno (1994), the rotating massive rectilinear segment (Riaguas, 1999; Riaguas et al., 2001), two perpendicular segments (Bartczak and Breiter, 2003; Bartczak et al., 2006), a rotating segment with variable density (Gutiérrez et al., 2024), or three spheres along a straight line (Palacios et al., 2019). By merging two of the above models, namely the dipole and segment, by adding the spheres of the dipole to the end points of the segment, Zeng et al. (2018) defined the Dipole-Segment model (DS) that has been used to describe the dynamics of several asteroids (Zeng and Liu, 2017; Zeng et al., 2018; Zhang et al., 2018; Elipe et al., 2021; Abad et al., 2024).

In the classical Circular Restricted Three Body Problem (RTBP) the angular velocity of the primaries is determined by their masses and the radius of the relative orbit of one around the other. At times, under the assumption that primaries are not spheric, other facts like the oblateness or their mutual orientation must be taken into consideration (Elipe, 2024; Elipe et al., 2024), but essentially, the angular velocity is determined by gravitation. However, in actual asteroid motions, the asteroid rotates depending on the initial conditions, and thus, there are asteroids with rotation faster than the RTBP, whereas other are slower. The rotation period is crucial in the origin and evolution of these small bodies, because many of them may be similar to the Itokawa as observed by Hayabusa spacecraft, that is to say, it looks like a rubble pile structure (Fujiwara et al., 2006); however, in order the particles on the asteroid surface remain on it, it is necessary a balance of the total forces acting on these particles. As Hirabayashi and Scheeres (2014) remark, when the spin rate is high, particles may fly off and do not immediately come back to the surface. In the three cases: the rotating dipole, the segment, and the DS models, there is a parameter κ given by Eq. (5) that is the ratio of the gravitational acceleration to centrifugal acceleration. When $\kappa < 1$, the segment experiences rapid rotation, whereas $\kappa > 1$ corresponds to slow rotation. As noted by Prieto-Llanos and Gómez-Tierno (1994), in rapidly rotating cases, cohesive strength is required to prevent structural disruption caused by inertial forces unbalanced by self-gravity. This consideration suggests that the regime $\kappa \ll 1$ is not physically realistic. Conversely, the slow-rotation regime appears to be the most prevalent, where a certain level of compressive strength prevents the body from collapsing into an oblate spheroidal configuration.

Besides, the value of this "force ratio" $\kappa$is also very important, because the dynamics of a particle orbiting around de DS strongly depends on the value of κ. For instance, for the dipole model ($\mu_s = 0$) for $\kappa > 1/8$ the problem has four equilibria, two triangular and other two collinear, but for $\kappa \leqslant 1/8$ there are no triangular equilibria and, consequently, the dynamics dramatically changes (Prieto-Llanos and Gómez-Tierno, 1994; Elipe et al., 2021). In Elipe et al. (2021) we make the exercice of computing some families of periodic orbits by fixing two of the parameters of the DS model, namely $\mu = 0.5$ (related with the ratio of the masses located at the end points of the segment) and the segment mass $\mu_s = 0.3$, whereas we use several values of κ. For values of $\kappa \leqslant 1$, the family choreographies are very similar each other, but as κ increases, there are many differences in which respect to the families and how they evolve and bifurcate. This fact motivates to make a complete analysis of symmetric periodic orbits of a real asteroid with slow rotation; among the possible candidates, we choose (25143) Itokawa (Fig. 1) because there are actual data obtained from the above mentioned Hayabusa mission. It orbits the Sun with period of 1.52 years at a distance between 0.95 and 1.70 AU, crossing the orbits of both Earth and Mars. It has a dipole-segment shape, and according to Zeng et al. (2018), its dimensions are $0.56 \times 0.30 \times 0.24$ km, with an equivalent radius of approximately 165 m, rotating about

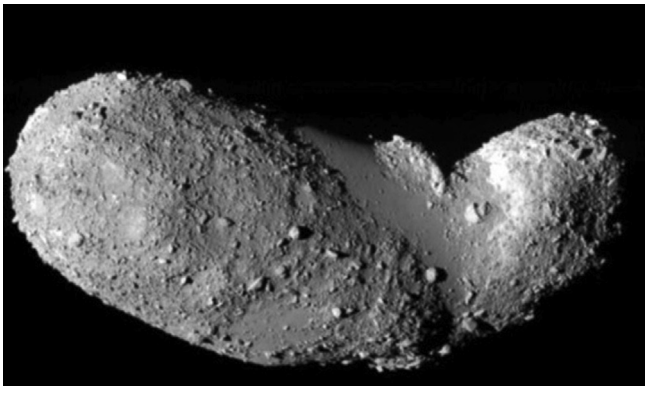

Fig. 1. Image of the asteroid Itokawa from the Hayabusa spacecraft (with permission of ISAS, JAXA).

its major principal axis of inertia with a period of 12.132 h, or equivalently $\kappa = 2.161$, greater that the unit.

At this point, let us mention that Zhang et al. (2018) systematically studied periodic orbits in the DS model and identified several types of three-dimensional periodic orbits for $\kappa = 1$. In contrast, the present work focuses exclusively on planar orbits for $\kappa > 1$, which exhibit a richer dynamical structure in terms of families of periodic orbits. Moreover, our study is complete in the sense that we identify all such families by scanning the plane of initial conditions and determine the stability of the orbits in each family.

The paper is organized as follows. In Section 2 we present a brief description of the formulation of the problem, that is, the notation used, parameters of the problem, potential function, and equations of motion, and also their equilibria and stability. In Section 3 we compute the heteroclinic orbits, that is to say, orbits connecting the unstable triangular orbits, as well as a short description on how to proceed for the computations. In Section 4 we compute the families of symmetric periodic orbits for the problem and make a topological characterization of them according to the classification give by Abad et al. (2023) and also we obtain the regions where each family is stable or unstable. Lastly, in Section 5 we make a comparison between the families of this problem with the ones of the RTBP; for each family, we compute several periodic orbits and see how they evolve depending on the value of the Jacobi constant. Additionally, in Appendix we present individual graphics of the 21 families of symmetric periodic orbits, together with their stability, and a table with numerical values of the stability intervals for each family.

2. Potential of the DS problem and equations of motion

Along the paper, we shall use the same notation as in previous works (Elipe and Riaguas, 2003; Riaguas et al., 2001; Zeng et al., 2018; Elipe et al., 2021; Abad et al., 2024), and the reader is addressed to these references for details. We just put here a short description of the different quantities and parameters used and the equations of motion we will use.

We define

$$M = m_1 + m_2 + m, \quad \mu = \frac{m_2}{m_1 + m_2},$$
$$(1-\mu) = \frac{m_1}{m_1 + m_2}, \quad \mu_s = \frac{m}{M}, \tag{1}$$

and denote by

$$(-\ell_1, 0, 0), \quad (\ell_2, 0, 0), \quad \text{with} \quad \ell_1 + \ell_2 = \ell$$

the coordinates of the masses m_1 and m_2 in the synodic frame $Oxyz$. With these definitons,

$$\frac{m_1}{M} = (1-\mu)(1-\mu_s), \quad \frac{m_2}{M} = \mu(1-\mu_s).$$

Note that if $\mu_s = 0$, there is no segment and this case corresponds to the classical Two-Center or Dipole Problem; when $\mu_s = 1$ ($\Longleftrightarrow m_1 = m_2 = 0$), only the segment remains. If $\mu = 0$ ($\Longleftrightarrow m_2 = 0$), there is only the mass m_1 at the left end of the segment, while if $\mu = 1$ ($\Longleftrightarrow m_1 = 0$) there is only the mass m_2 at the right end of the segment.

Because we assume that the origin O is at the center of mass of the system,

$$\frac{\ell_2}{\ell} = (1-\mu)(1-\mu_s) + \tfrac{1}{2}\mu_s, \qquad \frac{\ell_1}{\ell} = \mu(1-\mu_s) + \tfrac{1}{2}\mu_s, \tag{2}$$

and finally, the potential function is

$$U = -\mathscr{G}M\left(\frac{(1-\mu)(1-\mu_s)}{r_1} + \frac{\mu(1-\mu_s)}{r_2} + \frac{\mu_s}{\ell}\log\left[\frac{r_1 + r_2 + \ell}{r_1 + r_2 - \ell}\right]\right),$$

where $\mathscr{G}$ is the gravitation constant, $r_1 = \|P_1P\|$ and $r_2 = \|P_2P\|$, and thus,

$$r_1^2 = (x + \ell_1)^2 + y^2 + z^2, \quad r_2^2 = (x - \ell_2)^2 + y^2 + z^2.$$

After choosing the units in such a way that ℓ be the unit of length and $1/\omega$ the unit of time, the equations of motion in the synodic frame are

$$\begin{aligned} &\ddot{x} - 2\dot{y} = x - \tfrac{1}{\omega^2}\tfrac{\partial U}{\partial x} = \tfrac{\partial \Omega}{\partial x}, \\ &\ddot{y} + 2\dot{x} = y - \tfrac{1}{\omega^2}\tfrac{\partial U}{\partial y} = \tfrac{\partial \Omega}{\partial y}, \\ &\ddot{z} = -\tfrac{1}{\omega^2}\tfrac{\partial U}{\partial z} = \tfrac{\partial \Omega}{\partial z}, \end{aligned} \tag{3}$$

where Ω is the effective potential

$$\begin{aligned} \Omega &= \tfrac{1}{2}(x^2 + y^2) - \tfrac{1}{\omega^2}U \\ &= \tfrac{1}{2}(x^2 + y^2) + \kappa\left(\tfrac{(1-\mu)(1-\mu_s)}{r_1} + \tfrac{\mu(1-\mu_s)}{r_2} + \mu_s \log\left[\tfrac{r_1 + r_2 + 1}{r_1 + r_2 - 1}\right]\right), \end{aligned} \tag{4}$$

and the dimensionless parameter

$$\kappa = \frac{1}{\omega^2}\frac{\mathscr{G}M}{\ell^3} \in (0, \infty) \tag{5}$$

is the ratio of gravitational acceleration to centrifugal acceleration.

As occurs when the motion is described in a synodic frame, there is a first integral of Eqs. (3), the so-called Jacobi constant C given by

$$C = 2\Omega - (\dot{x}^2 + \dot{y}^2 + \dot{z}^2), \tag{6}$$

which yields significant information on the dynamical structure of the system, namely the zero-velocity curves and the associated forbidden regions of motion.

In the rest of the paper, we shall consider planar motions, consequently, in Eqs. (3) and (6) we put $z = 0$.

To apply the DS model to the (25143) Itokawa asteroid, we adopt the parameters reported by Zeng et al. (2018) for Itokawa, as summarized in Table 1.

With these values of the parameters, we compute the zero velocity surface $-C = -2\Omega(x, y)$ and the zero velocity curves that we represent in Fig. 2, showing graphically that there are four equilibria two collinear (L_1, L_2) and other two triangular (L_4, L_5). We compute the numerical values of the coordinates of the equilibria by zeroing Eqs. (3) and solving the resulting system, and also we compute

Table 1
Data of Itokawa after Zeng et al. (2018).

M	ℓ	ℓ_1	ℓ_2	T	κ	μ	μ_s
3.43×10^{10} kg	373 m	0.344312	0.655688	12.132 h	2.161	0.001	0.688

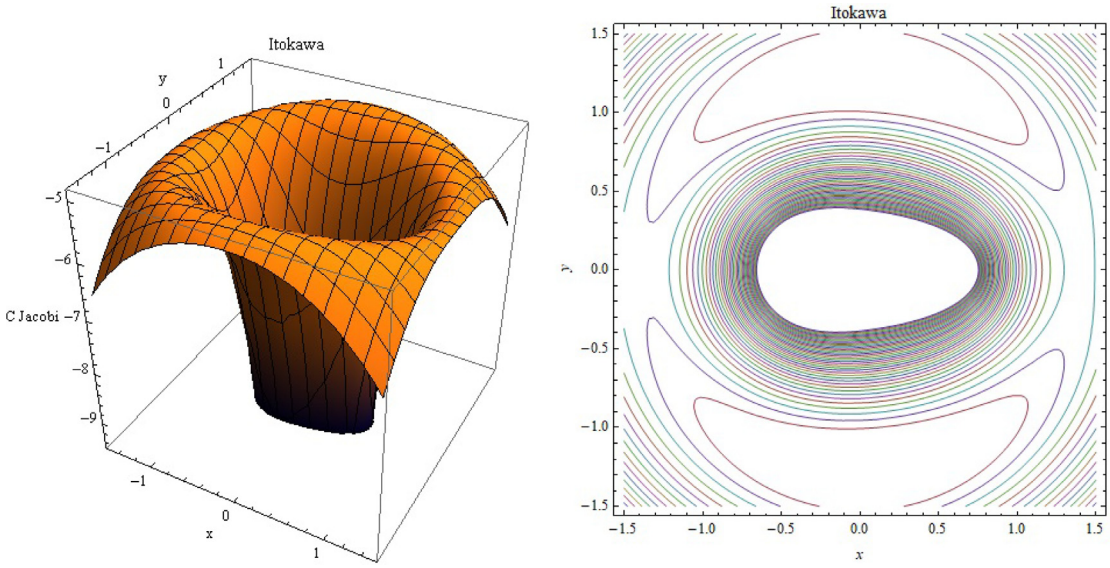

Fig. 2. Left: Zero velocity surface. Right: Zero velocity curve for the chosen parameters of Itokawa.

the stability of them by computing the eigenvalues of the linearized system. The results are in Table 2. Note that the equilibria L_1 is located to the left of the DS, that is, it corresponds to equilibrium L_3 in the RTBP.

3. Heteroclinic orbits

As above shown, triangular points L_i, $(i = 4, 5)$ of coordinates (x_T, y_T) are always unstable, and the solution of the planar linearized equations of motion can be written in the form

$$\begin{aligned} x(t) &= x_T + e^{\lambda_r t}(A_1 \cos\lambda_i t + A_2 \sin\lambda_i t) + e^{-\lambda_r t}(A_3 \cos\lambda_i t + A_4 \sin\lambda_i t), \\ y(t) &= y_T + e^{\lambda_r t}(B_1 \cos\lambda_i t + B_2 \sin\lambda_i t) + e^{-\lambda_r t}(B_3 \cos\lambda_i t + B_4 \sin\lambda_i t), \end{aligned} \tag{7}$$

where λ_r, λ_i are the real and imaginary parts of the eigenvalues of the variational matrix, and A_j, B_j $(j = 1, \ldots, 4)$ are constants of integration, but only four of them are independent, because constants B_j depend on constants A_j (see Szebehely (1967) §5.4.2). In consequence, an appropriate choice of constants A_j, B_j will provide orbits belonging either to the stable manifold

$$W^s(L_i) = \left\{ x \in \mathbb{R}^4,\ \lim_{t\to+\infty} \phi(t,x) \to L_i \right\}$$

or to the instable one

$$W^u(L_i) = \left\{ x \in \mathbb{R}^4,\ \lim_{t\to-\infty} \phi(t,x) \to L_i \right\},$$

where $\phi(t,x)$ denotes the flow passing though the point x.

The intersection of the stable and unstable manifolds $W^s(L_4) \cap W^u(L_5)$ contains those orbits going from L_5 to L_4 in infinity time; these orbits are stable in the sense that tend towards L_4, and will be denoted by $\mathscr{S}$. Conversely, the intersection $W^u(L_4) \cap W^s(L_5)$ is made of unstable orbits ($\mathscr{U}$) that is, orbits that leave L_4 towards L_5 in infinite time. Thus, these orbits connect in an infinity time two unstable equilibia, and were dubbed by Strömgren (1933) *solutions asymptotiques*, although later on they were known as heteroclinic orbits.

For computing heteroclinic orbits $\mathscr{S}$ and $\mathscr{U}$ we use the method given by Gómez et al. (1988) and also described in Abad et al. (2023). This method computes the manifold by propagating from Eqs. (7) the solution starting from initial conditions (x(0), y(0)) that describes a tiny circle

Table 2
Coordinates, stability and valaue of Jacobi constant of the equilibria for Itokawa.

	Coordinates	Eingvalues	Stability	$C(L_j)$
L_1	$(-1.36577, 0)$	$\pm 1.12469i \pm 0.653879$	Unstable	5.21451
L_2	$(1.39075, 0)$	$\pm 1.18117i \pm 0.809145$	Unstable	5.26623
L_4	$(0.0711189, 1.24918)$	$\pm 0.0779055i \pm 0.0326996$	Unstable	4.90645
L_5	$(0.0711189, -1.24918)$	$\pm 0.0779055i \pm 0.0326996$	Unstable	4.90645

around the triangular point; the propagation ends at the instant in which $y = 0$. Thus, we have a set of points $(x, 0, \dot{x}, \dot{y} = \dot{y}(x, \dot{x}; C))$ with C the Jacobian constant evaluated at the triangular equilibrium. Note that because of the symmetry, $C(L_4) = C(L_5) = C(T) = 4.906445$. In consequence, orbits of the stable ($\mathscr{S}$) or unstable ($\mathscr{U}$) manifolds can be represented on the plane $(x, \dot{x})$ because for then, $y = 0$ whereas $\dot{y}$ is determined by $x, \dot{x}$, and the Jacobian constant, as shown in Fig. 3 for both manifolds (stable on the left part and unstable on the right part of the plot). Even more, inasmuch as we are interested in symmetric orbits, from the sets of the found heteroclinic orbits we only select those satisfying $(x_h, \dot{x} = 0)$. In our case, we find six symmetric heteroclinic orbits, three of the type $\mathscr{S} : (\mathscr{S}_n, \mathscr{S}_p, \mathscr{S}_q)$ and other three of the type $\mathscr{U} : (\mathscr{U}_n, \mathscr{U}_p, \mathscr{U}_q)$ characterized by the following values of x_h:

	$\mathscr{S}_n$	$\mathscr{S}_p$	$\mathscr{S}_q$	$\mathscr{U}_n$	$\mathscr{U}_p$	$\mathscr{U}_q$
x_h	−2.448595	0.662267	0.670625	−0.403344	2.459934	2.739992

In Fig. 4 we plot the six heteroclinic orbits on the plane (x, y). On the left part the three orbits of the type $\mathscr{S}$, and on the right part the other three ones belonging to the type $\mathscr{U}$.

4. Symmetric periodic orbits around the asteroid Itokawa and their stability

4.1. Symmetric periodic orbits in the map (x_0, C_0).

It is worth to note than equations of motion (3) enjoy the symmetry $(t, x, y, \dot{x}, \dot{y}) \longrightarrow (-t, x, -y, -\dot{x}, \dot{y})$. This fact is very useful to compute periodic orbits that are symmetric with respect to the x-axis. Indeed, let us consider the initial

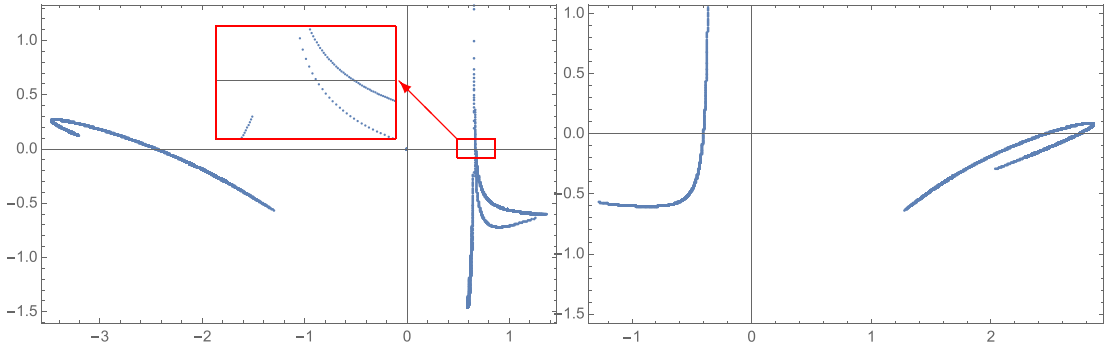

Fig. 3. Values $(x, \dot{x})$ of heteroclinic orbits belonging to the stable $\mathscr{S}$ (left) and unstable $\mathscr{U}$ (right) manifolds. Those orbits with $\dot{x} = 0$ are symmetrical, and we can see that there are six symmetric heteroclinic orbits, three stable and other three unstable.

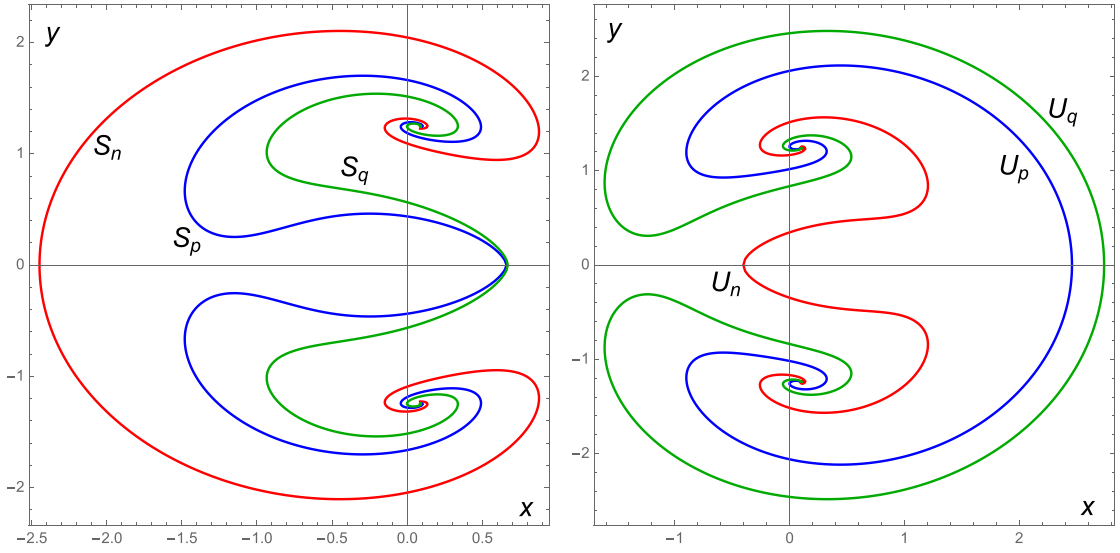

Fig. 4. Left: The three stable heteroclinic orbits $(\mathscr{S}_n, \mathscr{S}_p, \mathscr{S}_q) \in \mathscr{S}$, that is, orbits that arrive to L_4 from L_5 in infinity time. Right: The three unstable heteroclinic orbits $(\mathscr{U}_n, \mathscr{U}_p, \mathscr{U}_q) \in \mathscr{U}$, that leave L_4 towards L_5 in infinity time.

conditions $(x_0, y_0, \dot{x}_0, \dot{y}_0) = (x_0, 0, 0, \dot{y}_0)$ at the initial instant $t = 0$, and let us propagate the trajectory of Eqs. (3). With this, if there is an instant $t = T/2$at which the trajectory is $(x_{T/2}, 0, 0, \dot{y}_{T/2})$, we may conclude that the orbit is symmetric and periodic with period T. In other words, the semi-period $T/2$is the interval of time elapsed between two consecutive orthogonal crossings of the orbit by the x-axis.

Note that thanks to the existence of the Jacobian constant (6), there results that $\dot{y}_0 = 2\Omega(x_0, 0) - C_0$, which allows us to characterize a symmetric periodic orbit only by the pair (x_0, C_0). This is precisely the usual way to plot the collection of found symmetric periodic orbits, and also this set of coordinates (x, C) is employed in the so-called grid-search method that we use to find symmetric periodic orbits. This method is described in previous works, like (Markellos et al., 1974; Elipe et al., 2007; Palacios et al., 2019; Abad et al., 2023; Abad et al., 2024) and references therein.

What results interesting in using this representation to plot the set of periodic orbits (each point (x, C) corresponds to a symmetric periodic orbit) is that there are lines (see Fig. 5) called characteristic curves that represent the different families of periodic orbits (Strömgren, 1933; Hénon, 1997). Fig. 5 presents the characteristic curves for the values (Table 1) of the DS-model used for modelling Itokawa asteroid. In our case, we name f_n the different families; some of these families are related with the classical families of the Copenhagen problem (Strömgren, 1933; Hénon, 1965) and their classical notation appears in parentheses in Fig. 5, as well as in Table 3.

In order to distinguish the different families, we make a magnification of some areas, hence, we enlarge three zones Z_1, Z_1, and Z_3 that is also a zoom of a region of zone Z_3. These three zones are of particular interest, because they contain the so-called asymptotic or spiral points. Thus, in Z_1 we find the point $\mathcal{A}_n$, whereas in zone Z_3 there are

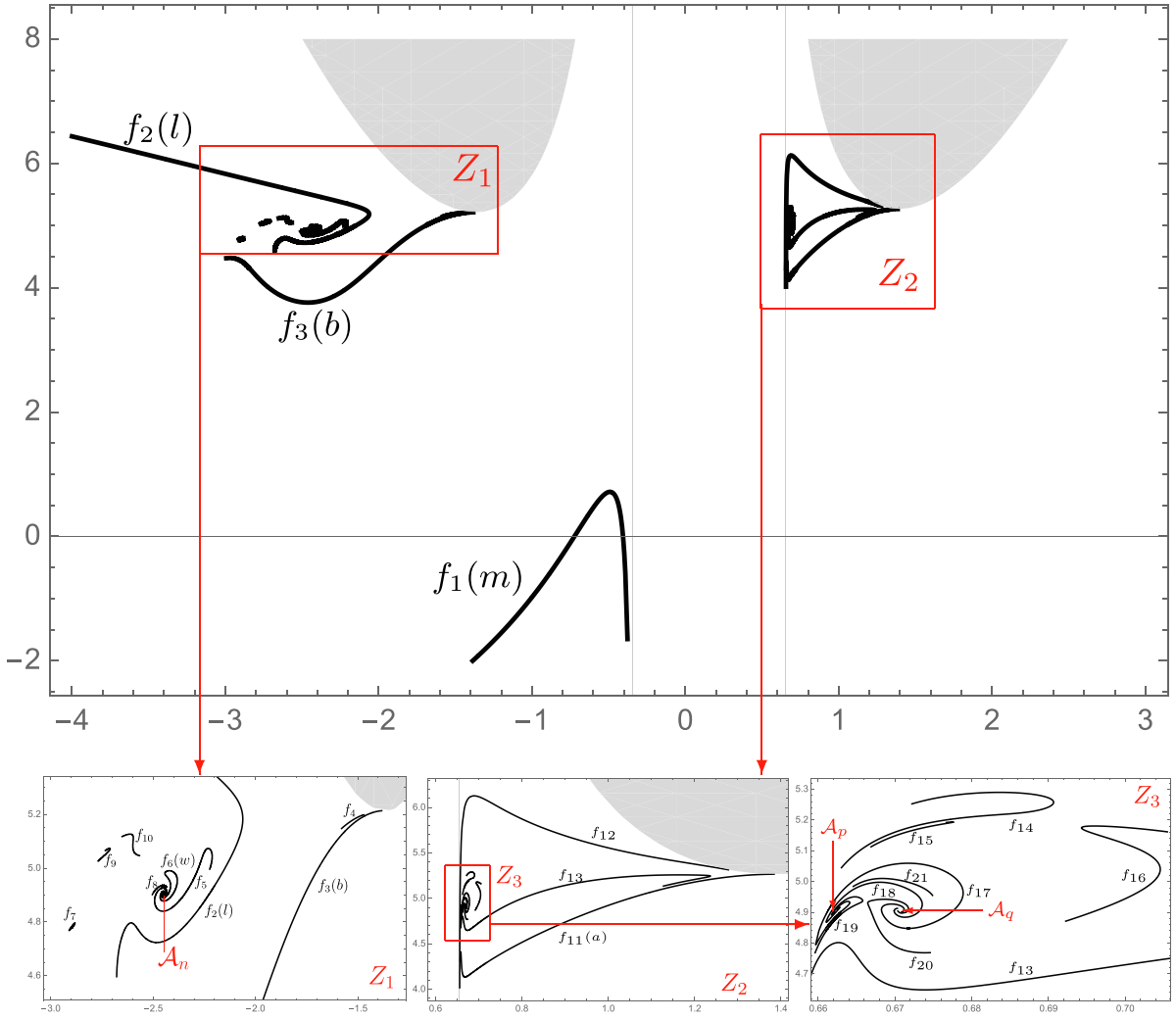

Fig. 5. Families of symmetrical periodic orbits of the asteroid Itokawa. Each point on the graphs in the (x, C) plane corresponds to the initial conditions of a periodic orbit, and each set of points forming a continuous curve represents a family, called f_n, for $n = 1, 2, 3, \ldots, 21$. The letter in parentheses in some cases after f_n represents the classic notation for families of the Copenhagen problem (Strömgren, 1933; Hénon, 1965). Shaded gray areas correspond to the forbidden motion regions. Magnifications of rectangles Z_1 and Z_2 highlighted in the main figure appear in the lower row of three plots. Region Z_3 is a zoom of a part of Z_2.

Table 3
Families of periodic orbits and their topological characterization

$f_1(m)$	$\mathscr{R}(\mathrm{DS})[\{L_1, L_2, T\} \rightarrow]$	$f_{11}(a)$	$\mathscr{R}(L_2)[\rightarrow T]$
		$f_{12}(j)$	$\mathscr{D}(\mathrm{DS})[\,]$
$f_2(l)$	$\mathscr{R}(L_1, \mathrm{DS}, L_2, T)[\,]$	$f_{13}(k)$	$\mathscr{D}(\mathrm{DS})[\rightarrow T]$
$f_3(b)$	$\mathscr{R}(L_1)[\rightarrow T]$	$f_{14}(j)$	$\mathscr{D}(\mathrm{DS})[\,]$
f_4	$\mathscr{R}(L_1, \mathrm{DS}, L_2, T)[\,]$	f_{15}	$\mathscr{R}(L_2, T)[\,]$
$f_5(u)$	$\mathscr{R}(L_1, T)[\rightarrow \mathscr{S}_n\mathscr{U}_n]$	f_{16}	$\mathscr{R}(L_2, T)[\,]$
$f_6(w)$	$\mathscr{R}(L_1, \mathrm{DS}, L_2, T)[\mathscr{S}_n\mathscr{U}_p \leftrightarrow \mathscr{S}_n\mathscr{U}_q]$	f_{17}	$\mathscr{D}(L_2, T)[\mathscr{S}_p\mathscr{U}_p \rightarrow \mathscr{S}_q\mathscr{U}_p]$
f_7	$\mathscr{R}(L_1, T)[\,]$	f_{18}	$\mathscr{R}(\mathrm{DS}, T)[\mathscr{S}_p\mathscr{U}_n \rightarrow \mathscr{S}_q\mathscr{U}_n]$
f_8	$\mathscr{R}(L_1, T)[\,]$	f_{19}	$\mathscr{D}(L_2, T)[\rightarrow \mathscr{S}_p\mathscr{U}_q]$
f_9	$\mathscr{R}(L_1, \mathrm{DS}, L_2, T)[\,]$	f_{20}	$\mathscr{D}(L_2, T)[\rightarrow \mathscr{S}_q\mathscr{U}_q]$
f_{10}	$\mathscr{R}(L_1, \mathrm{DS}, L_2, T)[\,]$	f_{21}	$\mathscr{R}(\mathrm{DS}, T)[\,]$

two asymptotic points $\mathscr{A}_p$ and $\mathscr{A}_q$ that are very close one another.

For the Copenhagen problem, Strömgren (1933) already suggested that for each pair of heteroclinic orbits, one of type $\mathscr{S}$ and the other of type $\mathscr{U}$, there is a family of periodic orbits that ends asymptotically at this pair of heteroclinic orbits. The end point of this family is precisely the spiral or asymptotic point above mentioned. This conjecture was proved by Henrard (1973) in Hamiltonian systems context. Recently, Abad et al. (2023) find the number of asymptotic points for each value of the mass parameter ($\mu \leqslant 0.5$) in the RTBP.

The name of spiral points comes from the fact that when represented the families on the plane (x, C), some of them tend in spiral shape towards the point (x_h, C_h) that corresponds to the orbits of type $\mathscr{S}$. At each one of these asymptotic points ends one family for each $\mathscr{U}$ orbit. For details, the reader is addressed to (Hénon, 1965; Abad et al., 2023).

In our case (see Fig. 5, bottom line), we find the following three asymptotic points of coordinates (x_h, C_h):

$$\begin{aligned} \mathscr{A}_n &= (-2.448595, 4.906445),\\ \mathscr{A}_p &= (0.662267, 4.906445),\\ \mathscr{A}_q &= (0.670625, 4.906445), \end{aligned}$$

and these points are the limits of some families of periodic orbits. Thus, families f_5 and f_6 end at the point $\mathscr{A}_n$. Families f_{17}, f_{18}, and f_{19} tends towards $\mathscr{A}_p$, whereas families f_{17}, f_{18}, and f_{20} go towards $\mathscr{A}_q$. It is noteworthy to remark that some families like f_5, f_{19}, and f_{20} finish at only one asymptotic point, but, on the contrary, both ends of families f_{17} and f_{18} finish at different spiral points, and even family f_6 starts and ends at the same spiral point $\mathscr{A}_n$. The pairs of stable ($\mathscr{S}$) and unstable ($\mathscr{U}$) heteroclinic orbits at which these families end appears in Table 3.

4.2. Topological characterization of orbits and families

In a recent paper, Abad et al. (2023) introduce a new notation to classify periodic orbits, in such a way that just the name of the orbit provides much information about the orbit; thus notation contains the direct ($\mathscr{D}$) or retrograde ($\mathscr{R}$) character of the orbit, what points (collinear (L_1, L_2), triangular (T) equilibria and/or the Dipole-Segment body) are surrounded by the orbit, and how periodic orbits evolve along their family. For details and a for a more complete description, see Abad et al. (2023).

In our case, we present on Table 3 the 21 families of symmetric periodic orbits $(f_1 \ldots . f_{21})$ with their corresponding topological characterization.

4.3. Stability

The stability of the orbits is given by the eigenvalues of the monodromy matrix (see e.g. Hénon (1965, 2005)) in such a way that the orbit is stable when the trace (tr) of this matrix is $-2 < \mathrm{tr} < +2$. With this, and with the only motivation of making a clear plot of the stability evolution along the family (see Figs. (6)), we take as stablity index the value $k = \log_2(|\,\mathrm{tr}\,|) - 1$, and consequently, the orbit is stable if $k < 0$.

To have an image of the stability of a chosen family (let us take for instance family f_{13}), we elaborate Fig. 6 with two plots. On the left, we plot the family on the plane of initial conditions (x_0, C_0). On the right, we plot the stability index k along the family, that is, we plot the curve $k = k(x_0, C_0))$. As said above, the family is stable for $k < 0$ (in orange), thus, we detect that there are three bands of stability, two very narrow strips on the left part of the plot, and another one, wider, on the right part. With this, we go back to the plot on the left and we mark with orange the portion of the family with stable orbits. The numerical limits of the stability regions of family f_{13} in the (x_0, C_0) map are presented in Table 4 (wtih only six decimal digits, as well as in Table 5; tables in Appendix appear with 15 decimal digits).

Now, let us take another family, namely the family f_{14}. For this family we repeat the same procedure as for family f_{13} and we find two regions where the family is stable.

Note that the curve of family f_{14} (as also happens with family f_{13}) has a vertical tangent point, that is, at a certain value of x_0 the curve goes from moving up to the right to moving up to the left. Moving along the family (in Fig. 7, left) we find the first interval of stability (the narrow one in orange with lower C_0); along this interval the initial condition x_0 increases, whereas in the second interval (the

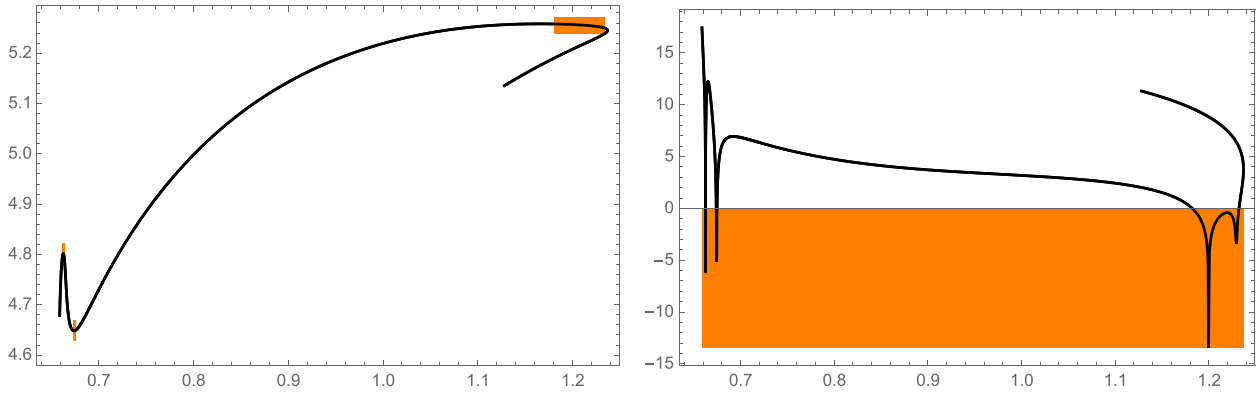

Fig. 6. Stability of family f_{13}. Left plot: Each point on the solid black line represents the initial conditions on the plane (x_0, C_0) of the f_{13} family orbits. The region highlighted in orange shows the initial conditions of the stable orbits. Right plot: It shows the stability index $k = k(x_0)$ of the orbits of the f_{13} family; note that the orbits are stable when $k < 0$, i.e., the region highlighted in orange.

Table 4
Stability intervals (x_0, C_0) of family f_{13}

First stable orbit		Last stable orbit
(0.662589, 4.801773)	→	(0.662617, 4.801792)
(0.674104, 4.648218)	→	(0.674875, 4.648555)
(1.182565, 5.257950)	→	(1.231663, 5.251208)

Table 5
Stability intervals (x_0, C_0) of family f_{14}

First stable orbit		Last stable orbit
(0.689099, 5.234371)	→	(0.689379, 5.236367)
(0.684194, 5.289847)	→	(0.685315, 5.289099)

wide orange with higher C_0) values of x_0 decrease as we move on the family curve; the values of the stability regions for family f_{14} appear in Table 5.

For the sake of avoiding overloading this section with 21 stability figures similar to the previous two ones, we include in the Appendix the corresponding figures and Tables A.1 and A.2 with the numerical values of the stability regions for the 21 families of symmetric periodic orbits in this problem. Let us mention that most part of the families are unstable as we can see in the Appendix.

5. Description of the families and their relation with the ones of the RTBP

Although different problems, both the Dipole-Segment and the Circular Restricted Three Body Problem present similarities and, in particular, some families of periodic orbits in the DS problem are related with the classical ones of the RTPB discovered by Strömgren (1933) and Hénon (1965) in the Copenhagen problem and later on extended by Abad et al. (2023) for all values of the mass parameter $(0 < \mu = m_2/(m_1 + m_2) \leqslant 0.5)$. This is why in the description of the families in the DS problem we shall make comparison with similar families of the RTBP. Note that orbits containing the asteroid (DS) are analogous to orbits that contain both primaries and the intermediate collinear equilibrium point $(P_1L_1P_2)$ in the RTBP.

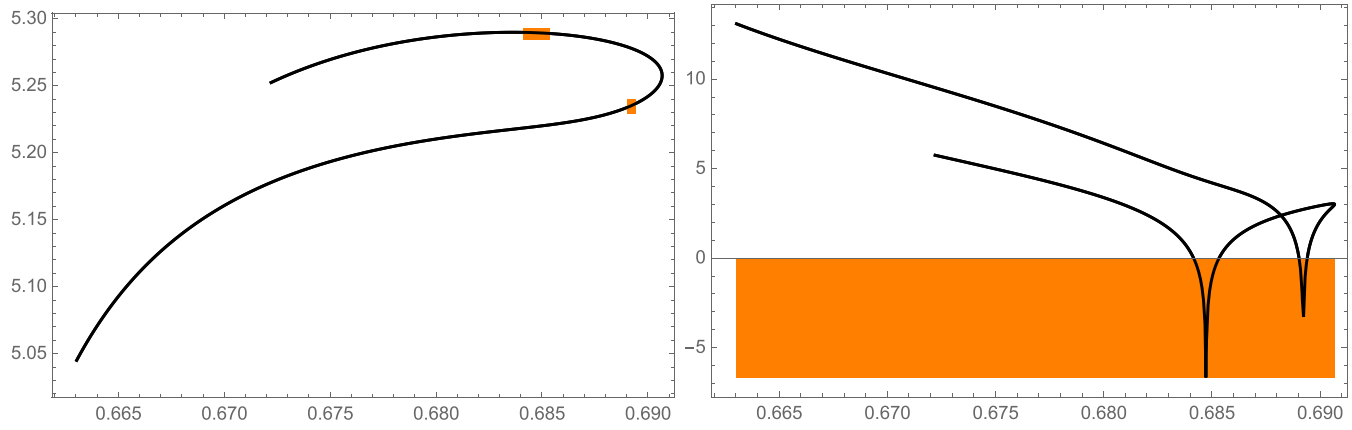

Fig. 7. Stability of family f_{14}. Left plot: the family f_{14} (the solid black line) on the plane (x_0, C_0); only the two narrow portions highlighted in orange correspond to stable orbits. Right plot: the stability index $k = k(x_0)$ along the family f_{14}; only orbits immersed in the orange band $(k(x_0) < 0)$ are stable, results that coincide with the one of the letf plot.

In order to have a snapshot of the behavior of the different families, for each family we plot several orbits $O_1, O_2, O_3, \ldots$ in ascending order along the family according to the following rule. Let $x_{0,j}$ be the initial condition of the symmetric periodic orbit O_j, obtained as described in the previous section. Then, we choose the order of the sequence of orbits $O_1, O_2, O_3, \ldots$ such that $x_{0,1} < x_{0,2} < x_{0,3} < \ldots$.

5.1. Family f_1

This family is identical to the classical family m and exists for all values of the three parameters (μ, μ_s, κ) of the DS problem, like in the cases studied in Elipe et al. (2021,). The orbits of this family are of the type $\mathscr{R}(\mathrm{DS})[\{L_1, L_2, T\} \rightarrow]$, that is, all orbits are retrograde and surround the DS; The first orbits of the family (O_1 in Fig. 8, left) also contains in its interior the four equilibria (L_1, L_2, T), and as the orbits approach the segment, they only contain the triangular, and eventually, all equilibria are outside the orbits (O_2, O_3, O_4, O_5 of Fig. 8, left). With regard to the stability of the orbits, all orbits until the one with initial conditions $(x, C) = (-0.510511, 0.704409)$ are stable and we draw them in red color. From this orbit until the end of the family, orbits are approaching to the DS (O_4, O_5) and are unstable.

5.2. Family f_2

Family f_2 is of the type $\mathscr{R}(L_1, \mathrm{DS}, L_2, T)[\,]$; that is, is made of retrograde orbits that always contain the asteroid and the four equilibria. Looking at this family in Fig. 5, it looks like family l in the Copenhagen problem. However, there is a big difference, because family l ends at an asymptotic point, whereas f_2 does not. Another difference with respect to the RTBP is that family in that problem bifurcate at a value $\mu = 0.12$ into a new family $\tilde{l}$ (see Fig. 13, right of Abad et al. (2023)) with the same characteristics that family f_2. Several orbits of this family are shown in Fig. 8 (right). Orbits in red (O_1, O_2, O_3) are stable; as a matter of fact, O_3 with initial conditions $(x, C) = (-2.332332, 5.432050)$ is the last stable orbit of the family. Beyond this value, the family becomes unstable, except for three very narrow zones as it is shown in the additional material file.

The shape of stable orbits O_1, O_2, O_3 is very similar to the stable ones of family f_1, but are more distant from the DS. As we progress along the family f_2, there appear two loops encircling the triangular points T (orbits O_4 in green and O_5 in blue), although they do not approach the asymptotic point $\mathscr{A}_n$.

5.3. Families f_3, f_{11} and f_4

Family f_3 is identical to family b of the Copenhagen problem. It is represented in Fig. 9 (center). It is of the type $\mathscr{R}(L_1)[T \rightarrow]$, that is, made of retrograde orbits that always contain the collinear point L_1. Besides, at the beginning of the family, the orbits also encircle the triangular points (orbits O_1, O_2) but at a certain value of the initial conditions, orbits become of halo type around L_1. Note also that the first orbit O_1, which is stable, very much approach to the DS and to the point L_2.

The family f_{11} (in zone Z_2 of Fig. 5) is of the type $\mathscr{R}(L_2)[\rightarrow T]$ and it is identical to family a of the Copenhagen problem. It is represented in Fig. 9 (right), and its orbits look like to be symmetric to those of family f_3.

Family f_4 is very short (see zone Z_1 of Fig. 5), and it is very close to family f_3. Orbits are of the type $\mathscr{R}(L_1, \mathrm{DS}, L_2, T)[\,]$. Indeed, its orbits (Fig. 9, left) start on the Ox-axis at a point very close to L_1, but they quickly move away encircling points T, L_2 and the body DS; then, the orbit comes back towards L_1, making a small loop and

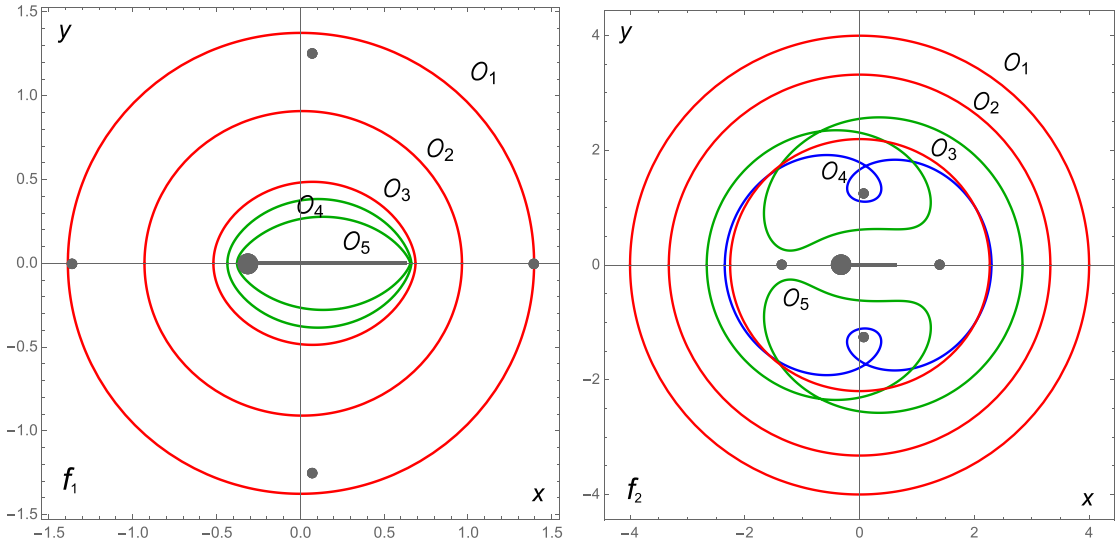

Fig. 8. Left: orbits of the family f_1. Right: orbits of the family f_2. Orbits in red color are stable, whereas other colors are used for unstable orbits.

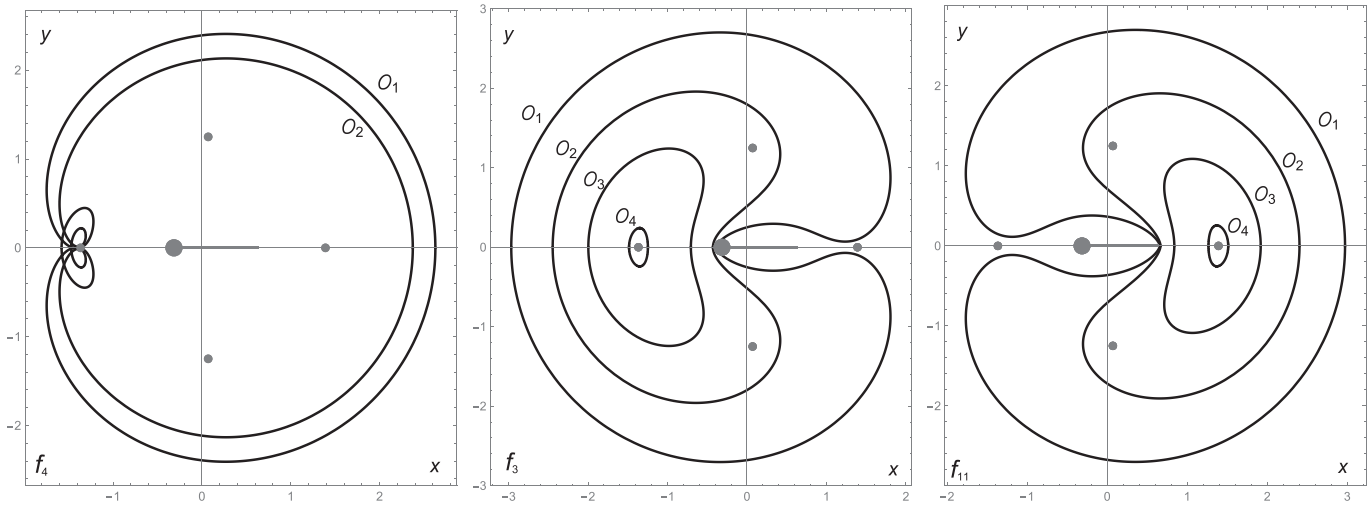

Fig. 9. Orbits of families f_4 (left), f_3 (center), and f_{11} (right). Note that there is no code color for stable orbits from here on.

encircling it. This family is very similar to family $\tilde{l}_2$ that appears in the RTBP for very small values of the mass parameter ($\mu = 0.08$); see Fig. 15 of Abad et al. (2023). Let us remark that from here one, red color does not mean that the orbit is stable.

5.4. Families f_{12}, f_{13} and f_{14}

These three families are made of direct orbits that surround the Dipole-Segment DS. Families f_{12} and f_{14} are of the type $\mathscr{D}(\mathrm{DS})[\,]$, whereas f_{13} is of the type $\mathscr{D}(\mathrm{DS})[T \rightarrow]$. In Fig. 10 we present several orbits of these families. On the left, family f_{12}; family f_{14} in the center; and family f_{13} on the right. Note that the first orbits of f_{13} look like orbits of f_{12} and f_{14}, but the last ones (O_1, O_2) also surround the triangular points.

In comparison with the RTBP, the classical families k, and j that cuts each other for $\mu = 0.50$ but that are separated for $\mu < 0.50$, are quite similar to families f_{12}, f_{13} and f_{14}. In particular, f_{12} and f_{14} are similar to family j, whereas f_{13} is similar to family k.

5.5. Families ending at an asymptotic point

As we already said, there are six families $(f_5, f_6, f_{17}, f_{18}, f_{19}$ and $f_{20})$ that end at some of the three asymptotic points $\mathscr{A}_n, \mathscr{A}_p$, and $\mathscr{A}_q$. In particular, families f_5 and f_6 arrive to point $\mathscr{A}_n$. Family f_5, similar to classic family u, is of the type $\mathscr{R}(L_1, T)[\rightarrow \mathscr{S}_n\mathscr{U}_n]$, that is, retrograde, and surrounds the equilibria L_1 and triangular points T. This family starts at $\mathscr{A}_n$ as the union of two heteroclinic orbits $\mathscr{S}_n\mathscr{U}_n$. On the left part of Fig. 12 we present several orbits of this family, and we may compare these orbits with the union of orbits $\mathscr{S}_n$ and $\mathscr{U}_n$ of Fig. 4.

Family f_6 ($\mathscr{R}(L_1, \mathrm{DS}, L_2, T)[\mathscr{S}_n\mathscr{U}_p \leftrightarrow \mathscr{S}_n\mathscr{U}_q]$) is similar to the classical retrograde family w, surrounds all equilibria and the dipole-segment, and both ends finish at the same asymptotic point $\mathscr{A}_n$ in such a way that one end-point finishes at the $\mathscr{S}_n\mathscr{U}_p$ union, whereas the other ends at $\mathscr{S}_n\mathscr{U}_q$ (see Fig. 4). We draw several orbits of this family on the left part of 11.

As it can be seen in Fig. 5, points $\mathscr{A}_p$ and $\mathscr{A}_q$ are very close one another, and thus, the four families ending at

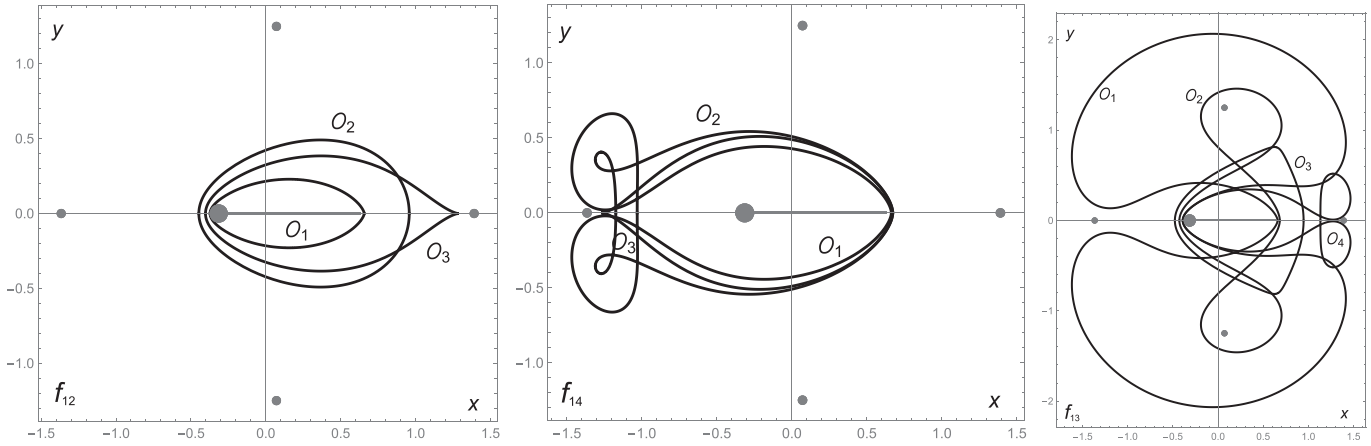

Fig. 10. Orbits of families f_{12} (left), f_{14} (center), and f_{13} (right).

them are quite short. These families have no counterpart in the RTBP because in that problem there is only one asymptotic point to the right of both primaries.

Both end-points of families f_{17} and f_{18} start and end at different points. Thus, they start in $\mathscr{A}_p$ and finish at $\mathscr{A}_q$. Family $f_{17}$is of type $\mathscr{D}(L_2,T)[\mathscr{S}_p\mathscr{U}_p \to \mathscr{S}_q\mathscr{U}_p]$, that is to say, direct orbits surrounding L_2 an the triangular equilibria T, besides, the orbits start in $\mathscr{S}_p\mathscr{U}_p$ and end at $\mathscr{S}_q\mathscr{U}_p$ (see central plot of Fig. 11).

On the other hand, family f_{18} is of the type $\mathscr{R}(\mathrm{DS},T)[\mathscr{S}_p\mathscr{U}_n \to \mathscr{S}_q\mathscr{U}_n]$, that is, orbits are retrograde, surround the Dipole-Segment (DS) and the triangular equilibria T. These orbits start in $\mathscr{S}_p\mathscr{U}_n$ and end at $\mathscr{S}_q\mathscr{U}_n$, as we can see in Fig. 11 (right part). Very close to this family f_{18} there is another family, f_{21}, very short and its orbits that surround the (DS) and the triangular equilibria T, look very much like central orbits of family f_{18}.

Lastly, f_{19} and f_{20} end at an asymptotic point, but only at one of their end-points. Family f_{19} is of the type $\mathscr{D}(L_2,T)[\to \mathscr{S}_p\mathscr{U}_q]$, because its orbits are direct, and surround L_2 and triangular (T) equilibria points and eventually end at the asymptotic point $\mathscr{A}_p$ with the union of $\mathscr{S}_p\mathscr{U}_q$ orbits (see central part of Fig. 12).

Family f_{20} is of the type $\mathscr{D}(L_2,T)[\to \mathscr{S}_q\mathscr{U}_q]$, that is, its orbits are very similar to the ones of family f_{19}, but now the family ends at the asymptotic point $\mathscr{A}_q$ with the union of $\mathscr{S}_q\mathscr{U}_q$ orbits (see right part of Fig. 12).

5.6. Other families

Finally, let us mention that in this problem we find other families (of short length) that are not directly related with classic families and that present no special characteristics. From their topological characterization we find three different types. Families f_7 and f_8 are of the type $\mathscr{R}(L_1,T)[\,]$, as their close families $f_3(b)$ and $f_5(u)$. Families f_9 and f_{10} are of the type $\mathscr{R}(L_1,\mathrm{DS},L_2,T)[\,]$ alike families $f_2(l)$ and $f_6(w)$. Lastly, families f_{15} and f_{16} are of the type $\mathscr{R}(L_2,T)[\,]$, that is to say, their orbits are direct and enclose

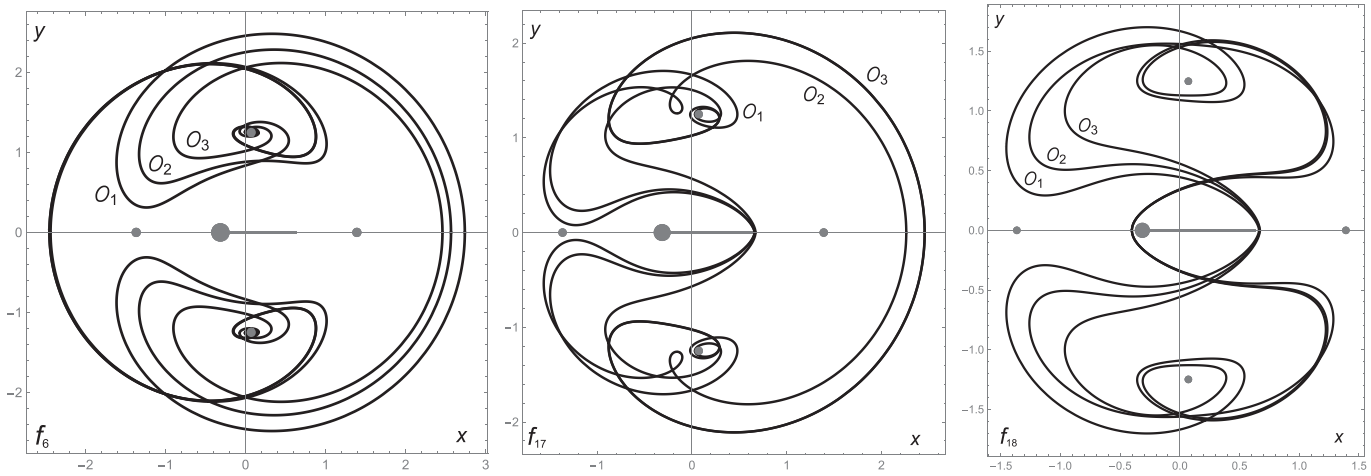

Fig. 11. Families f_6, f_{17}, and f_{18} ending at asymptotic points.

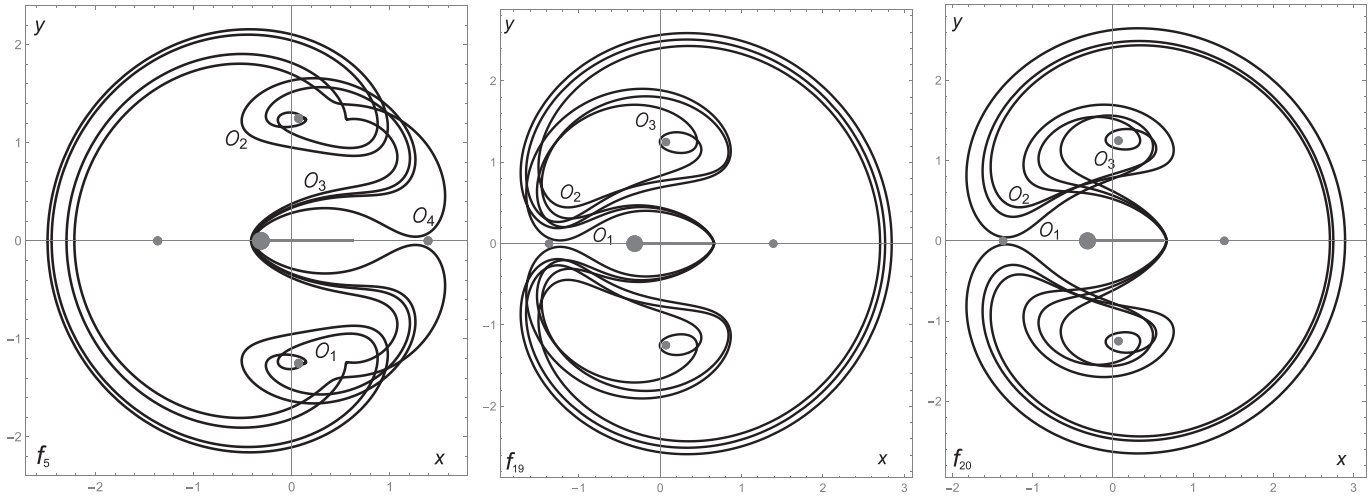

Fig. 12. Families f_5, f_{19}, and f_{20} that end at an asymptotic point, but only at one end-point of the family.

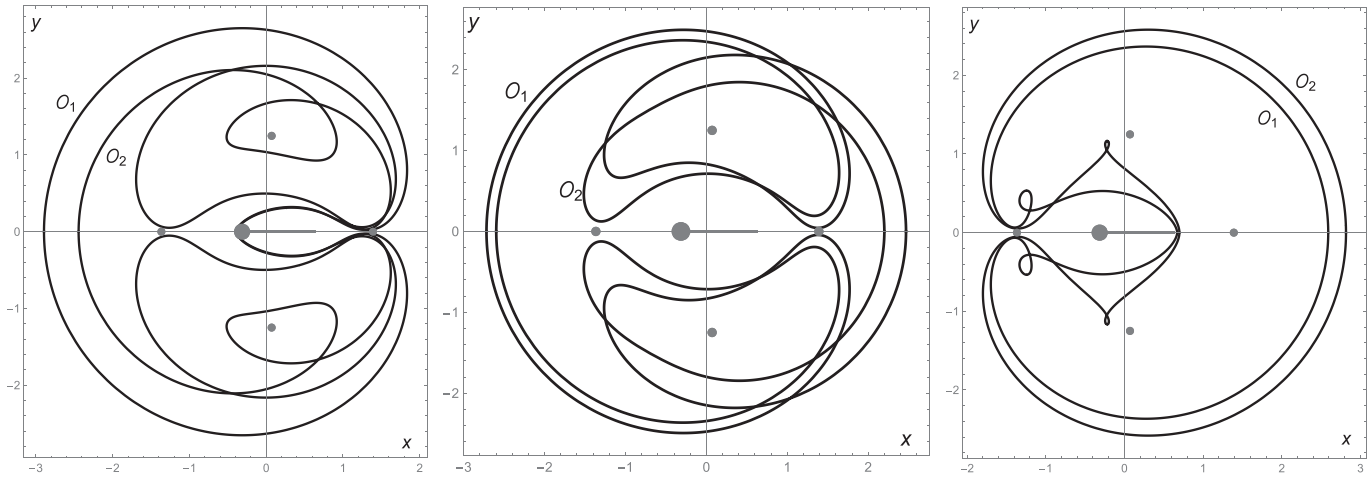

Fig. 13. One orbit of each of the remaining families. Left: $O_1 \in f_7$, $O_2 \in f_8$. Center: $O_1 \in f_9$, $O_2 \in f_{10}$. Right: $O_1 \in f_{15}$, $O_2 \in f_{16}$.

equilibria L_2 and T, similarly to the retrograde families f_{17}, f_{19}, and f_{20}.

In Fig. 13 we present one orbit of each of these families. In the left plot, orbit O_1 belongs to family f_7, whereas O_2 belongs to family f_8. Center plot shows orbit O_1 belonging to family f_9 and orbit O_2 of family f_{10}. Plot on the right contains orbit O_1 of family f_{15} and orbit O_2 of f_{16}.

6. Conclusions

In this work, we investigated the planar dynamics around the Dipole-Segment (DS) model applied to the asteroid (25143) Itokawa, focusing on the slow-rotation regime characterized by $\kappa = 2.161$. The DS model provides a computationally efficient and closed-form representation of elongated bodies with end-point protrusions, offering physical consistency with the rubble-pile structure inferred for Itokawa.

We identified all symmetric periodic orbit families associated with this configuration, obtaining 21 families and providing a systematic topological characterization of their evolution. Their linear stability was evaluated through the monodromy matrix, revealing that only a limited number of orbits remain stable within narrow parameter intervals. This finding highlights that stable regions are scarce in the vicinity of slow-rotating elongated bodies.

Additionally, we detected six heteroclinic orbits between unstable triangular equilibria and demonstrated that three spiral (asymptotic) points organize the transitions between several families. These global dynamical structures indicate the existence of natural transport pathways that may facilitate low-energy motion near the asteroid.

Overall, our study shows that slow-rotating DS-type bodies exhibit a significantly richer and more intricate dynamical landscape than moderate- or fast-rotating cases previously reported. The dynamical maps, stability analysis, and heteroclinic structures reported here may serve as a valuable reference for future trajectory design and close-proximity operations around Itokawa-like asteroids.

Declaration of competing interest

The authors declare that they have no known competing financial interests or personal relationships that could have appeared to influence the work reported in this paper.

Acknowledgments

The authors are grateful to the anonymous reviewers for their constructive criticism and valuable suggestions. This work has been supported by Grant PID2024-156002NB-I00 funded by MICIU/AEI/10.13039/501100011033/FED ER, UE, by FAPESP #2023/11781–5, and by the Aragon Government and European Social Fund (group E24-26R).

Appendix A. Stability of all families

As it was explained in SubSection 4.3, we define the stability index as $k = \log_2(|\mathrm{tr}|) - 1$, where "tr" denotes the trace of the monodromy matrix. An orbit is stable when $k < 0$.

For each family, we proceed in the same way; therefore, the explanation given for one family applies equally to all 21 families. Each figure in this appendix contains two plots. The left plot shows the considered family in the (x_0, C_0) plane, extracted from Fig. 5. The right plot, in the (x_0, k) plane, displays a horizontal band (in orange) together with the evolution of the stability index $k = k(x_0)$ the family. When this curve lies within the orange band, the orbit with initial condition (x_0, C_0) is stable; otherwise, it is unstable.

Using this criterion, we identify the stable intervals and mark the corresponding regions along the family in orange in the left plot. In this way, we can easily see that families f_4, f_{15}, an f_{19} are unstable everywhere. Other families, such as f_1 and f_2, are composed mainly of stable orbits, whereas the remaining families are unstable almost everywhere.

In Tables A.1 and A.2 we present in detail the initial conditions (x_0, C_0) of the first and last stable orbits in each stability interval for every family.

Figs. A.1,A.2,A.3,A.4,A.5,A.6,A.7,A.8,A.9,A.10,A.11, A.12,A.13,A.14,A.15,A.16,A.17,A.18,A.19,A.20,A.21

Table A.1
Stability intervals (x_0, C_0) of families f_1 to f_{13}

First stable orbit		Last stable orbit
Family f_1		
	→	(−0.510510510510510, 0.70440908282470)
Family f_2		
	→	(−2.332332332332332, 5.43205042930694)
(−2.477443609022556, 4.72347886095846)	→	(−2.457393483709273, 4.72588893521470)
(−2.610807552126887, 4.79639639639639)	→	(−2.608771929824561, 4.79663357970336)
(−2.625512835592683, 4.78828828828828)	→	(−2.623429677234147, 4.79009009009009)
Family f_3		
(−2.993606891058917, 4.47477477477477)	→	(−2.991891891891892, 4.475273471052604)
(−2.974024024024024, 4.47845535529655)	→	(−2.970870870870871, 4.478600454304703)
(−2.437437437437437, 3.76324146368839)	→	(−2.282389080560335, 3.875875875875876)
Family f_4		
	Unstable everywhere	
Family f_5		
(−2.45026026026026, 4.92734287807474)	→	(−2.44994494494494, 4.927340025717038)
(−2.45165165165165, 4.83989349231391)	→	(−2.45060060060060, 4.839916094725409)
(−2.23003003003003, 5.07338023536816)	→	(−2.22732732732733, 5.072995255808355)
Family f_6		
(−2.448631831831832, 4.914009021808231)	→	(−2.448585585585585, 4.914008831326185)
(−2.447749674606518, 4.877466176617785)	→	(−2.447277777777778, 4.877472835377611)
(−2.413813813813814, 4.990010608704785)	→	(−2.412012012012012, 4.989675908119674)
(−2.420420420420420, 4.990636206342458)	→	(−2.418018018018018, 4.990516064538319)
(−2.448788788788789, 4.892078263423889)	→	(−2.448578578578578, 4.892080823663310)
(−2.448615075376884, 4.910512927378289)	→	(−2.448600150753769, 4.910512885750667)
Family f_7		
(−2.8831896517654454, 4.795491098301454)	→	(−2.8831682995566275, 4.795503188128612)
Family f_8		
(−2.4503552753653355, 4.936024913571885)	→	(−2.4503256208902275, 4.936024887170976)
(−2.4497100645883094, 4.936018653740727)	→	(−2.4496808229259224, 4.936018084851019)
Family f_9		
(−2.7124549846288977, 5.073841484412026)	→	(−2.7122793148880104, 5.073845644800200)
(−2.7173060200668897, 5.072874866585382)	→	(−2.7171086956521737, 5.072933157542366)
Family f_{10}		
(−2.6128062480165357, 5.1268837435320425)	→	(−2.6125725482247217, 5.126884947503305)
Family f_{11}		
(0.668848848848849, 4.135190227771123)	→	(0.671021021021021, 4.137949277576205)
(0.674944944944945, 4.147809837403744)	→	(0.681827738194850, 4.170470470470471)
Family f_{12}		
(0.6946946946946948, 6.125480273409407)	→	(0.7453423451155592, 6.008008008008009)
Family f_{13}		
(0.662589255922589, 4.80177294285202)	→	(0.662616928666451, 4.801792203486513)
(0.674104104104104, 4.64821786496037)	→	(0.674874874874875, 4.648554934365585)
(1.182565130260521, 5.25794978083669)	→	(1.231663326653307, 5.251207655912418)

Table A.2
Stability intervals (x_0, C_0) of families f_{14} to f_{21}

First stable orbit		Last stable orbit
Family f_{14}		
(0.689099099099099, 5.234371049989798)	→	(0.689379379379379, 5.236367159670478)
(0.684194194194194, 5.289846895784466)	→	(0.685315315315315, 5.289098968720479)
Family f_{15}		
	Unstable everywhere	
Family f_{16}		
(0.6960234425326199, 5.180570436593818)	→	(0.6960982296861074, 5.180564685317558)
(0.6979781863488932, 5.179118166078727)	→	(0.6980458308549652, 5.179032517020424)
Family f_{17}		
(0.6713013013013013, 5.059430872739069)	→	(0.6715815815815815, 5.059587640403580)
(0.6719135564137084, 4.847956521739130)	→	(0.6719349456588702, 4.847973244147157)
Family f_{18}		
(0.6679090339619052, 4.99783588117416)	→	(0.6679462720887115, 4.99785202776499)
Family f_{19}		
	Unstable everywhere	
Family f_{20}		
(0.6687391353578617, 4.942552625826422)	→	(0.6687930711649615, 4.942528363579602)
(0.6686660897398661, 4.942571409501379)	→	(0.6686981697901508, 4.942565148276393)
(0.6739087572420905, 4.768721180312614)	→	(0.6740765007431675, 4.768753503978242)
Family f_{21}		
(0.6682124166582735, 5.010156942694547)	→	(0.6682330815664149, 5.010163555395321)

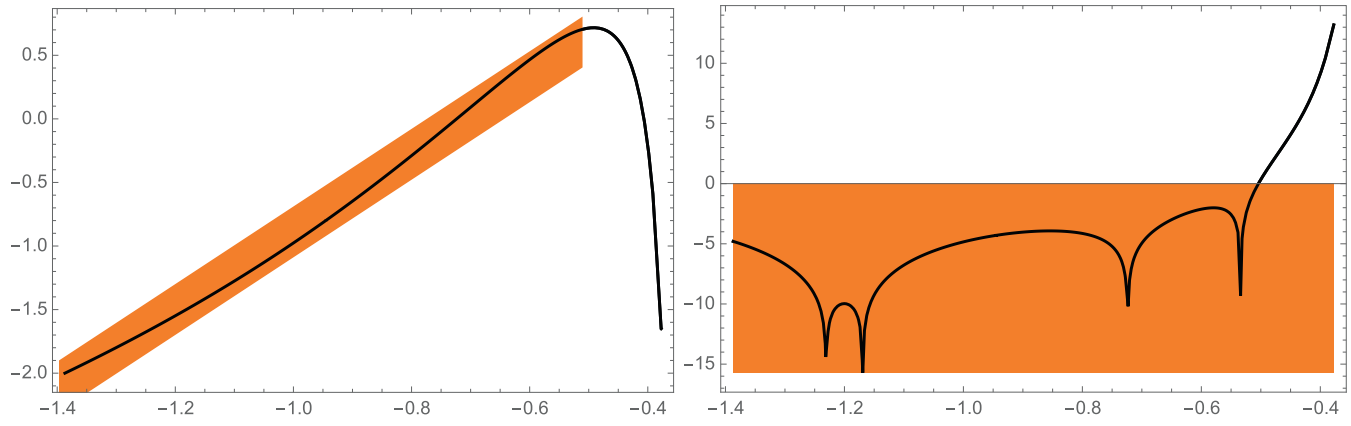

Fig. A.1. Family f_1.

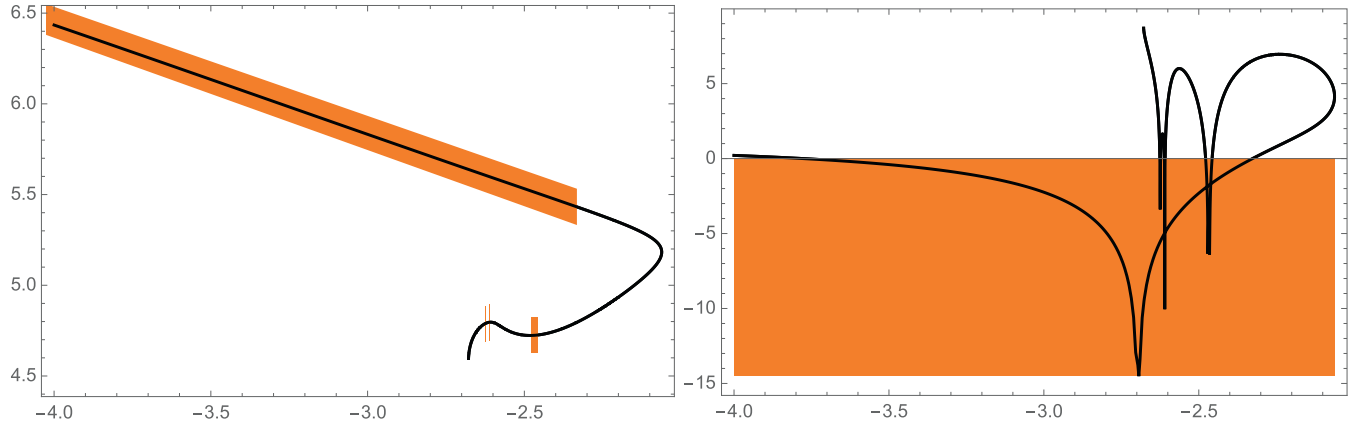

Fig. A.2. Family f_2.

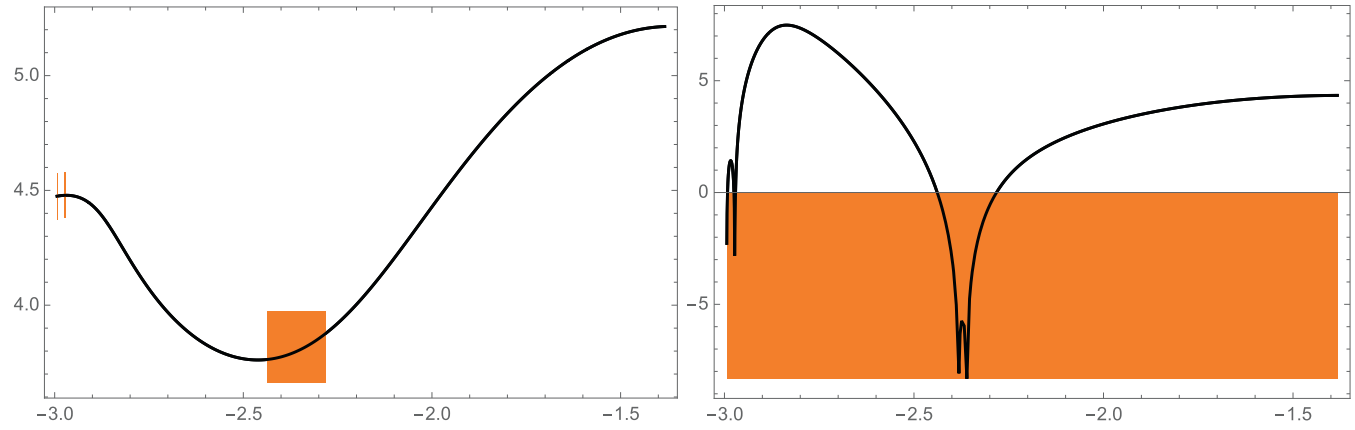

Fig. A.3. Family f_3.

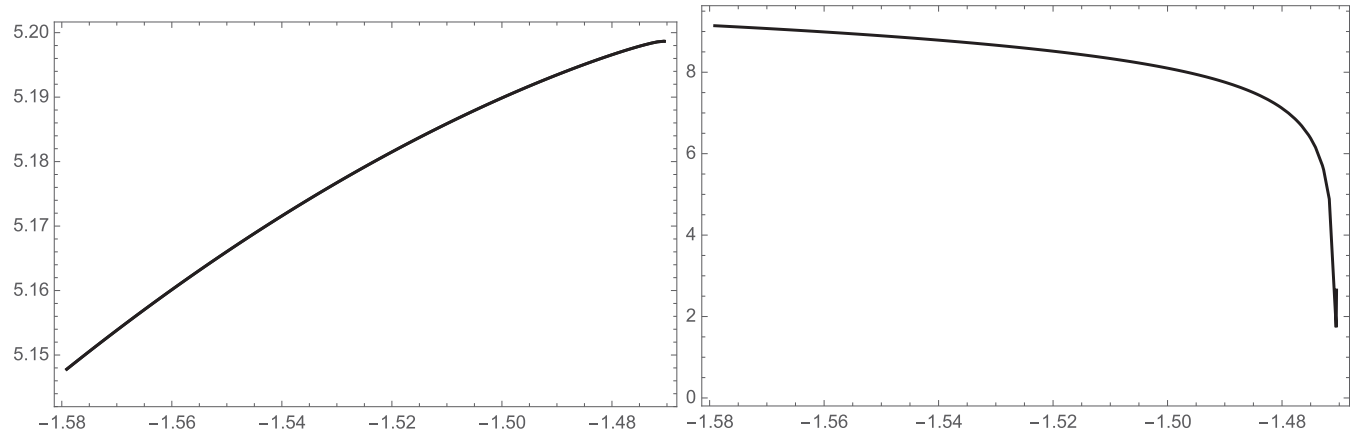

Fig. A.4. Family f_4.

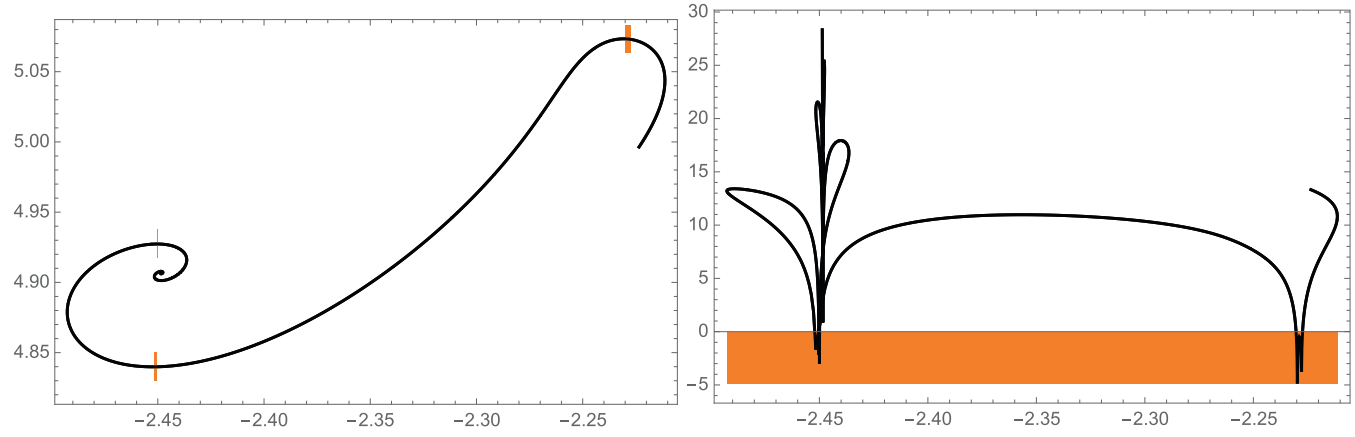

Fig. A.5. Family f_5.

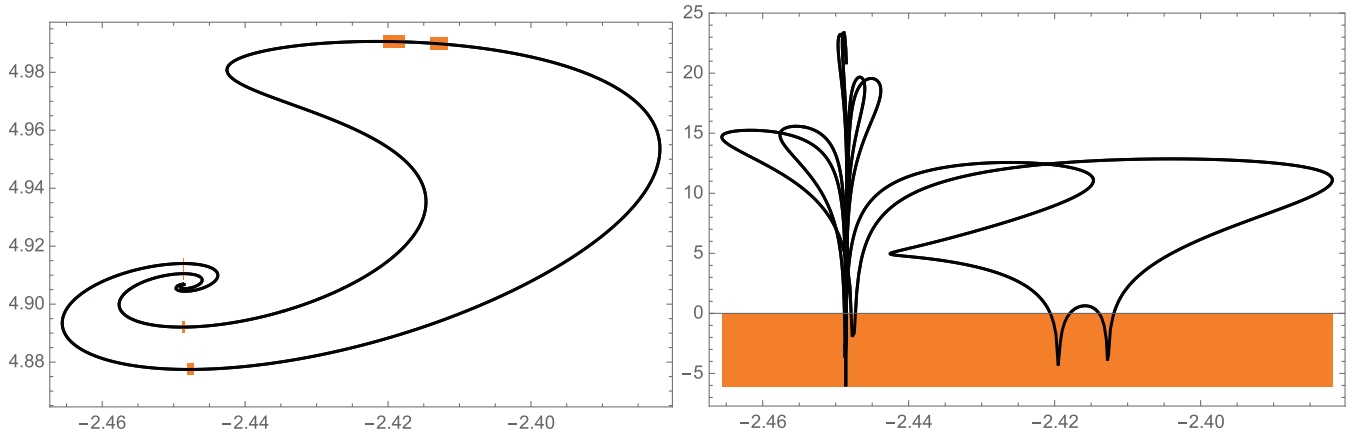

Fig. A.6. Family f_6.

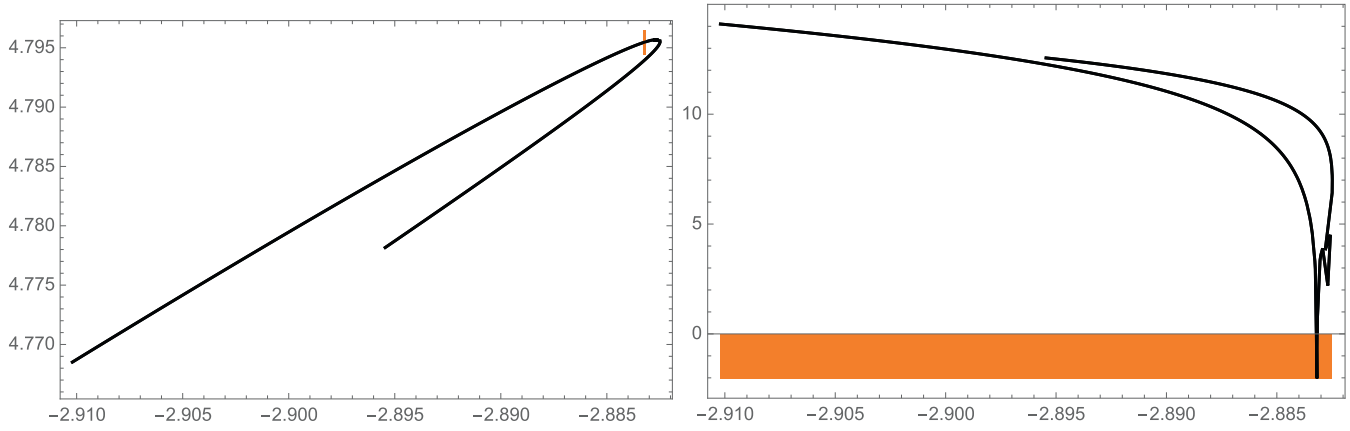

Fig. A.7. Family f_7.

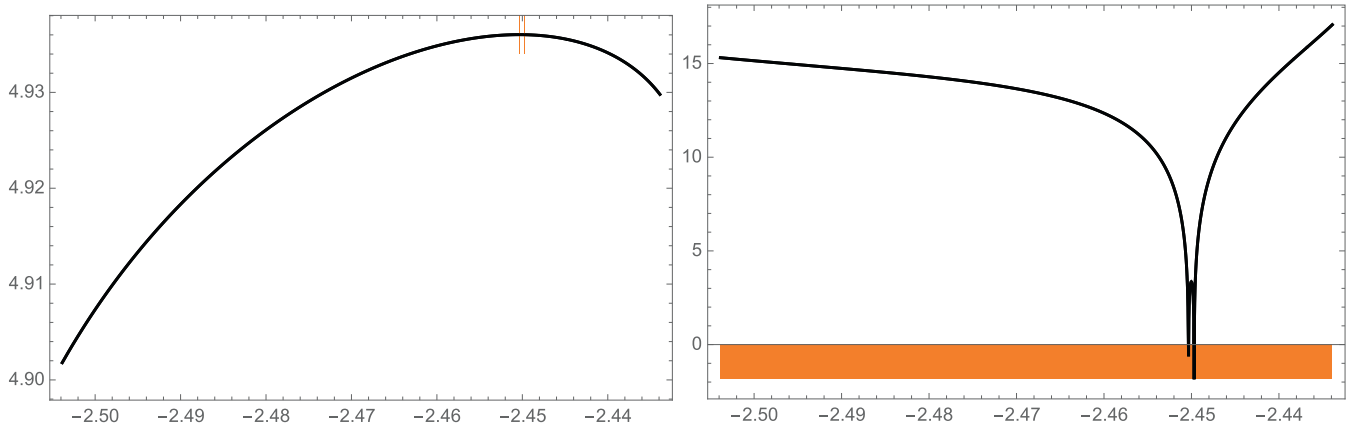

Fig. A.8. Family f_8.

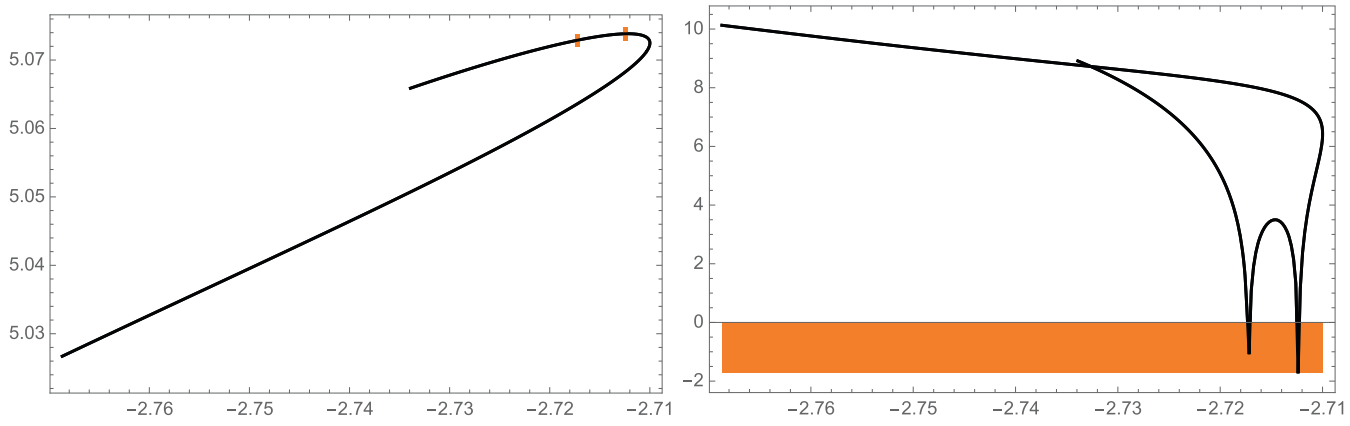

Fig. A.9. Family f_9.

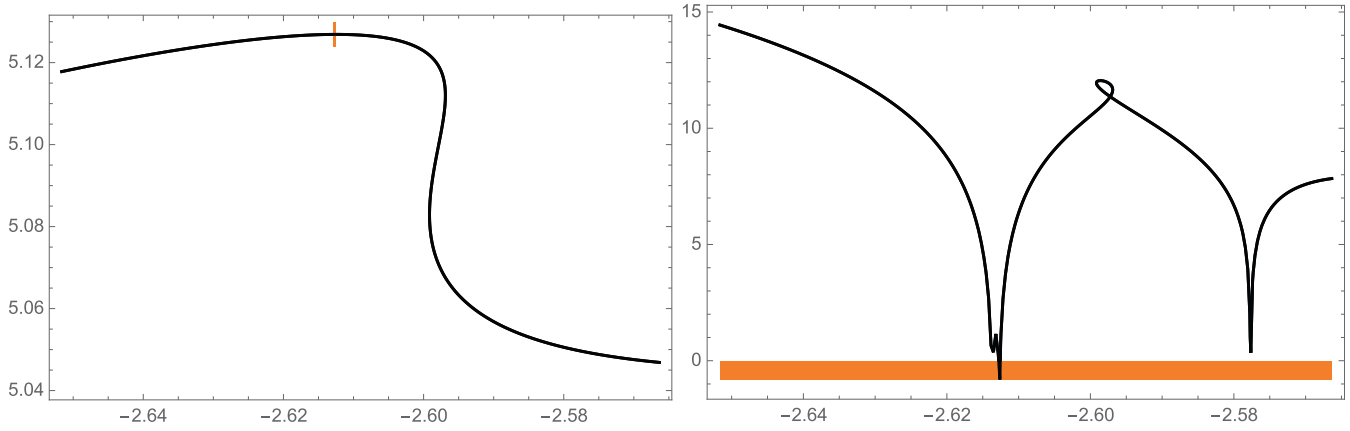

Fig. A.10. Family f_{10}.

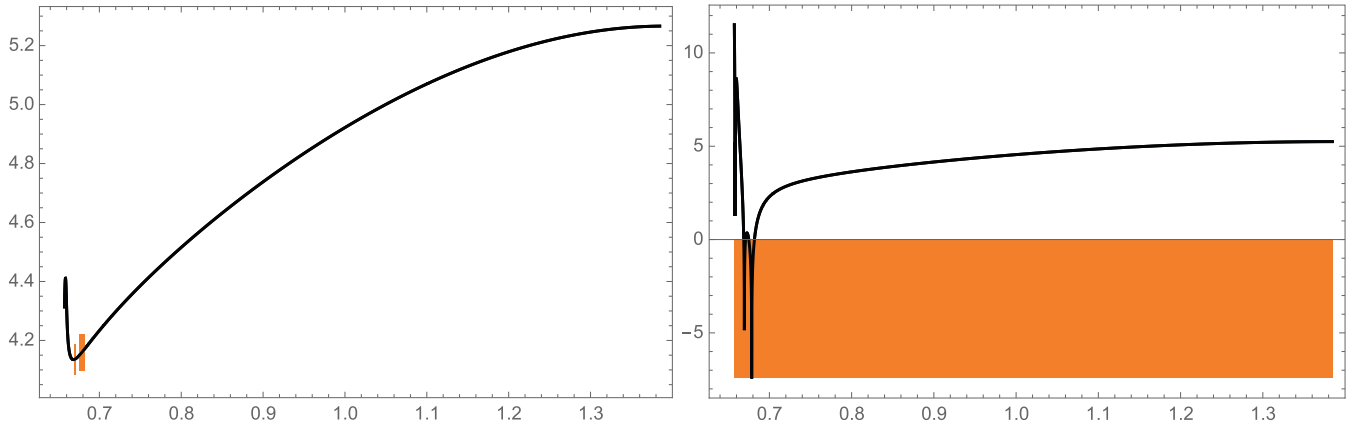

Fig. A.11. Family f_{11}.

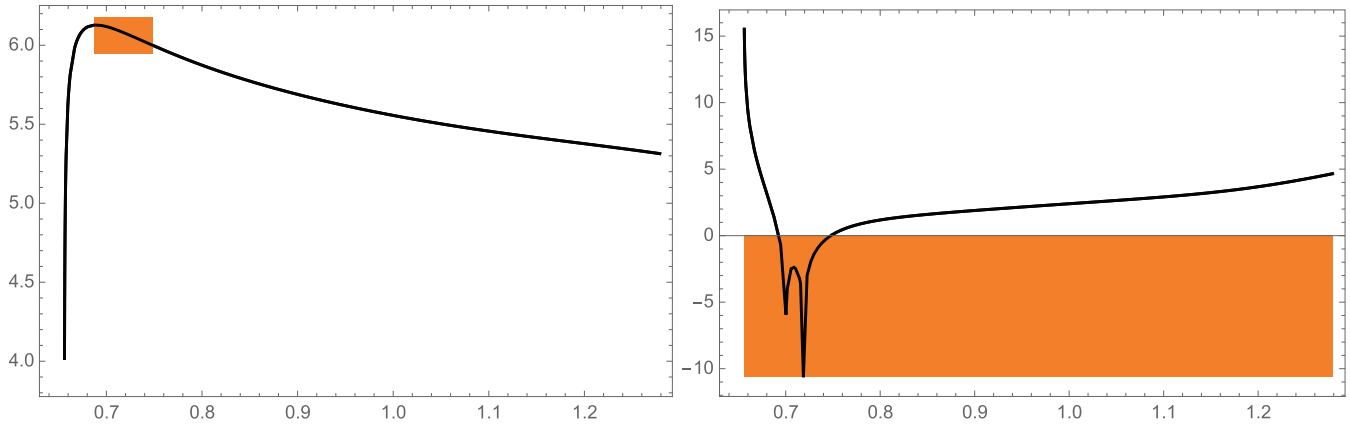

Fig. A.12. Family f_{12}.

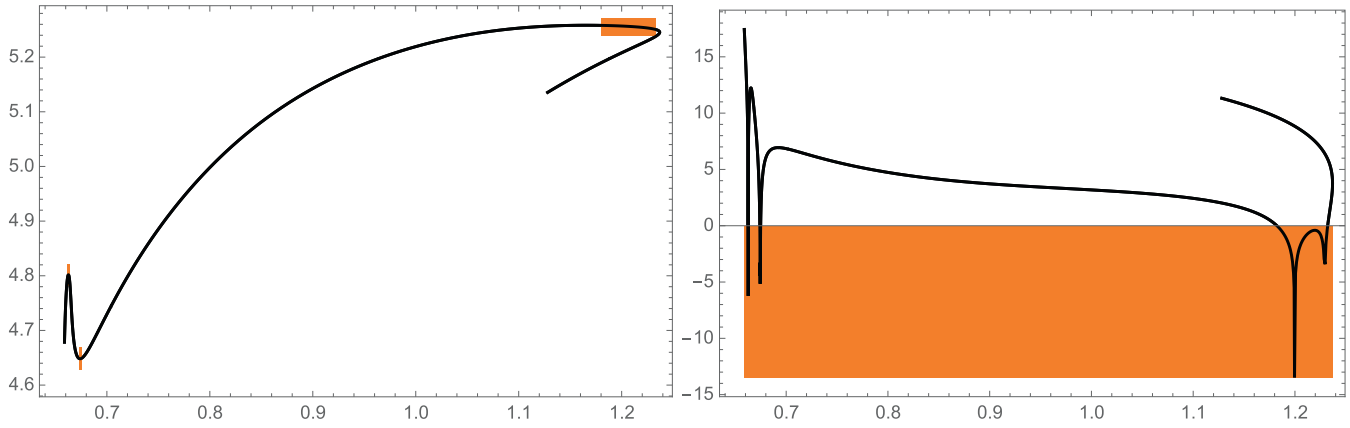

Fig. A.13. Family f_{13}.

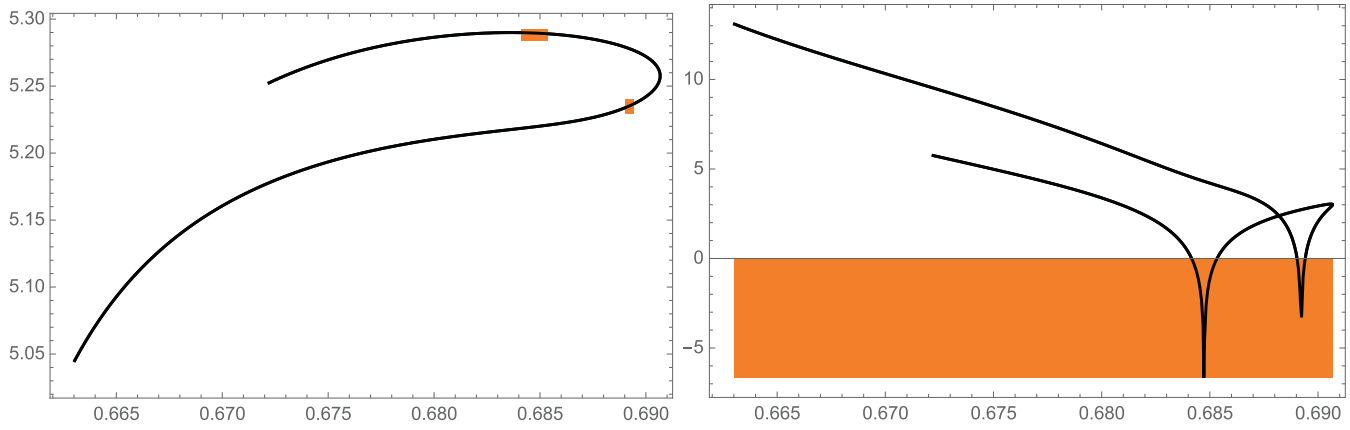

Fig. A.14. Family f_{14}.

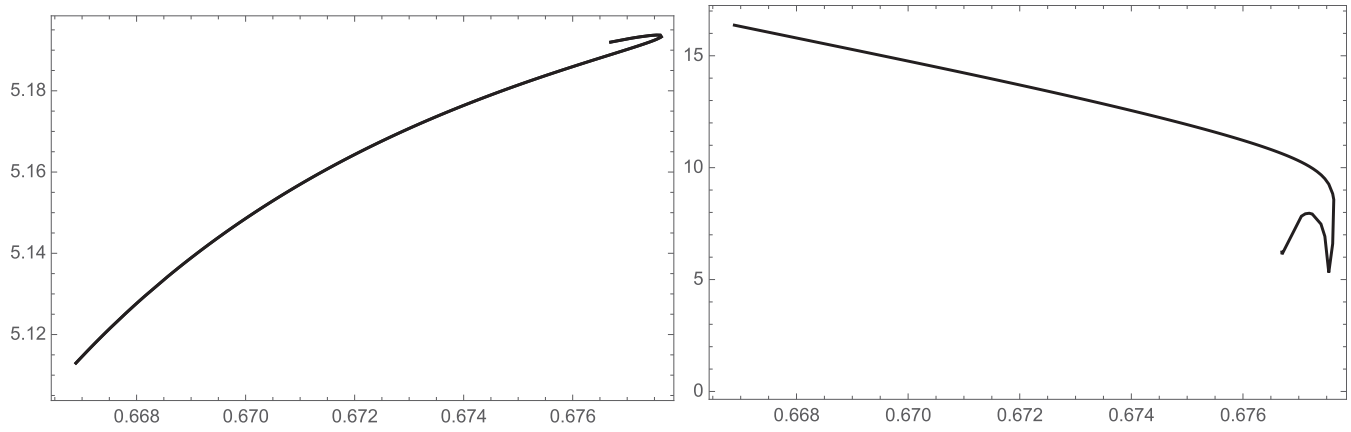

Fig. A.15. Family f_{15}.

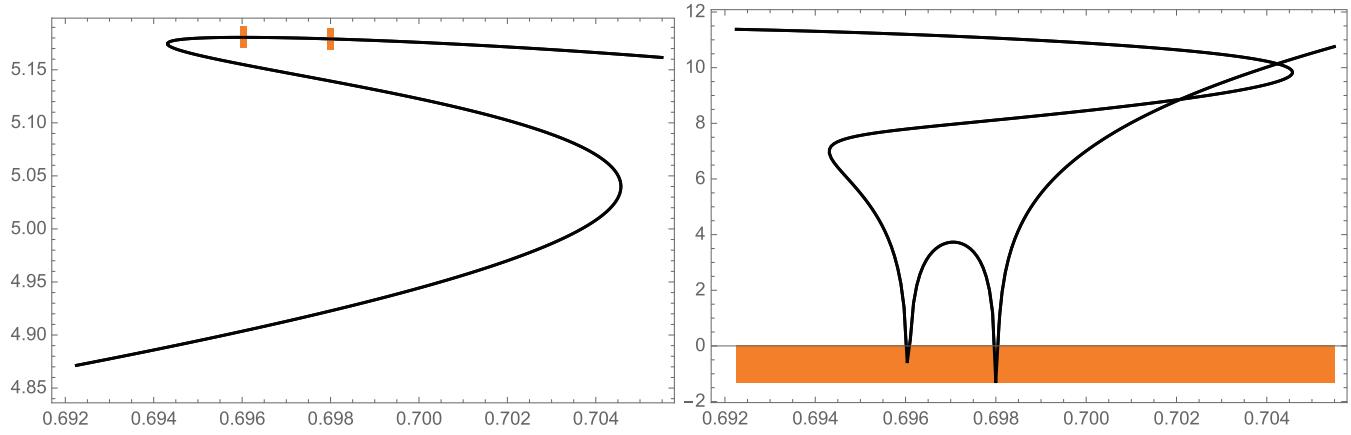

Fig. A.16. Family f_{16}.

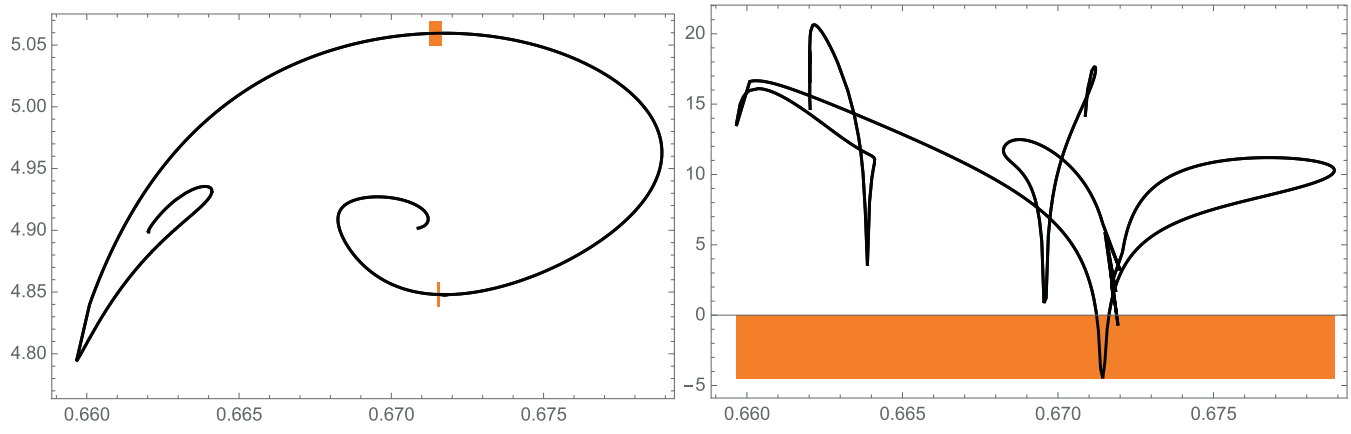

Fig. A.17. Family f_{17}.

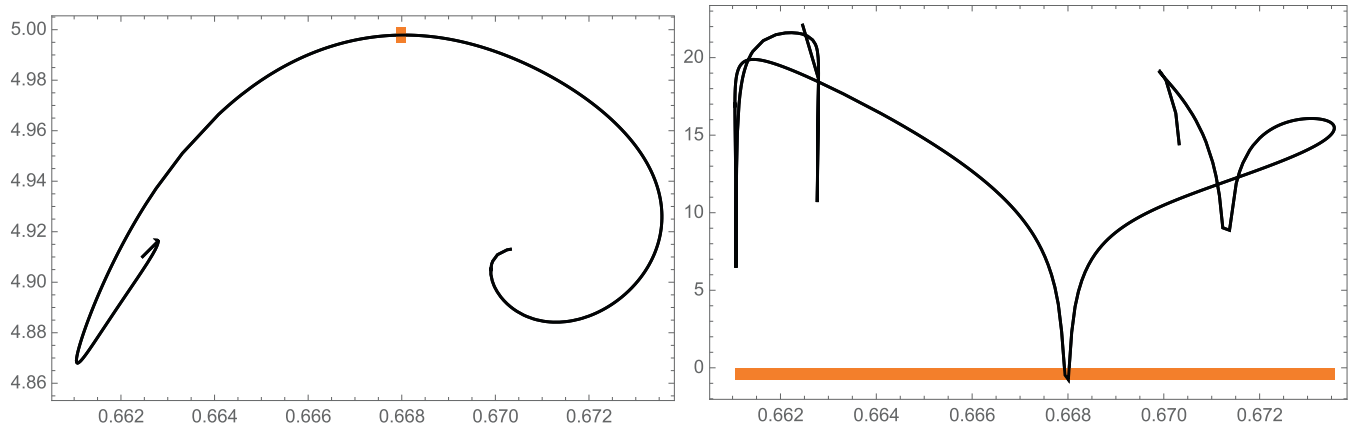

Fig. A.18. Family f_{18}.

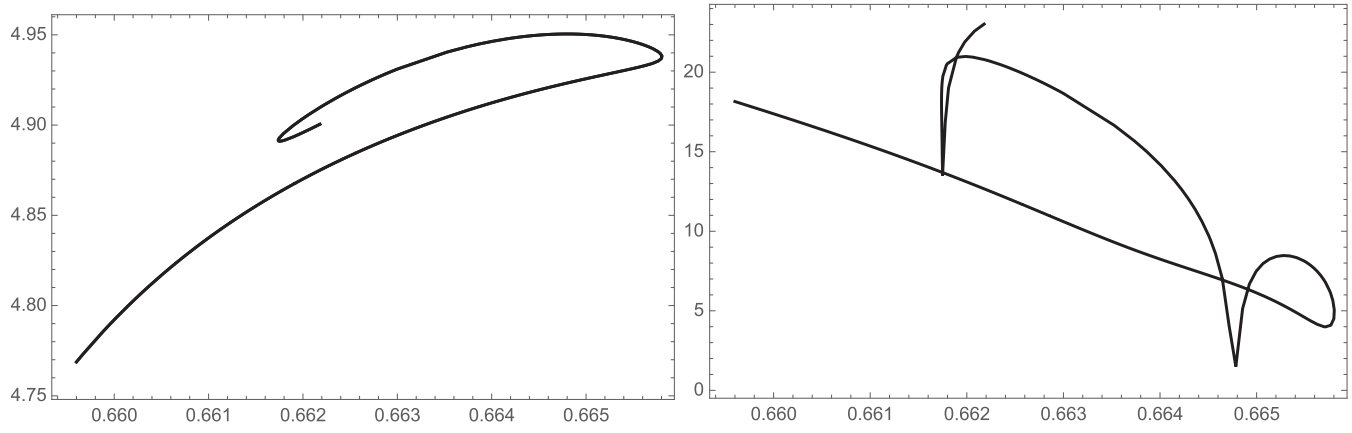

Fig. A.19. Family f_{19}.

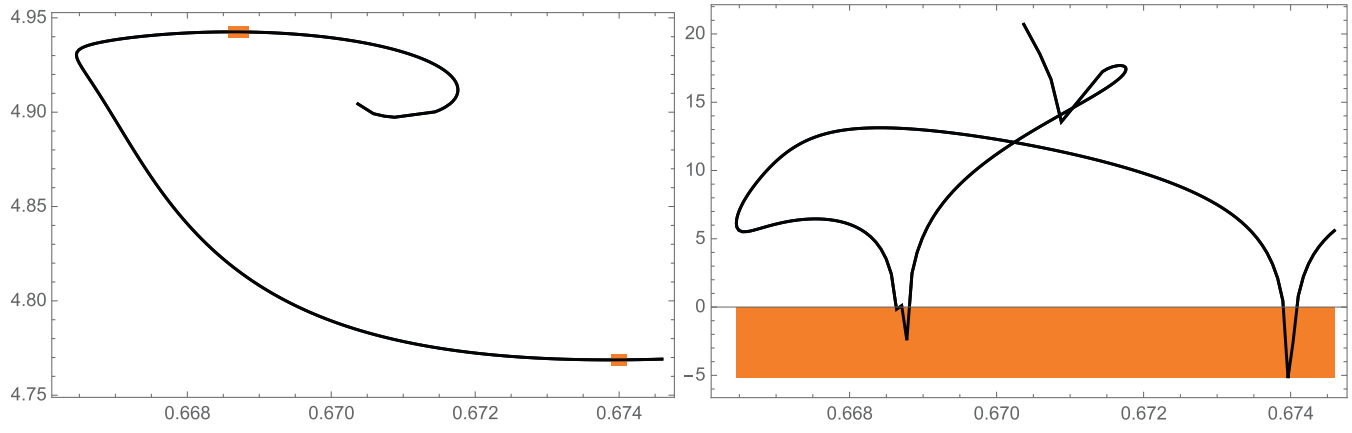

Fig. A.20. Family f_{20}.

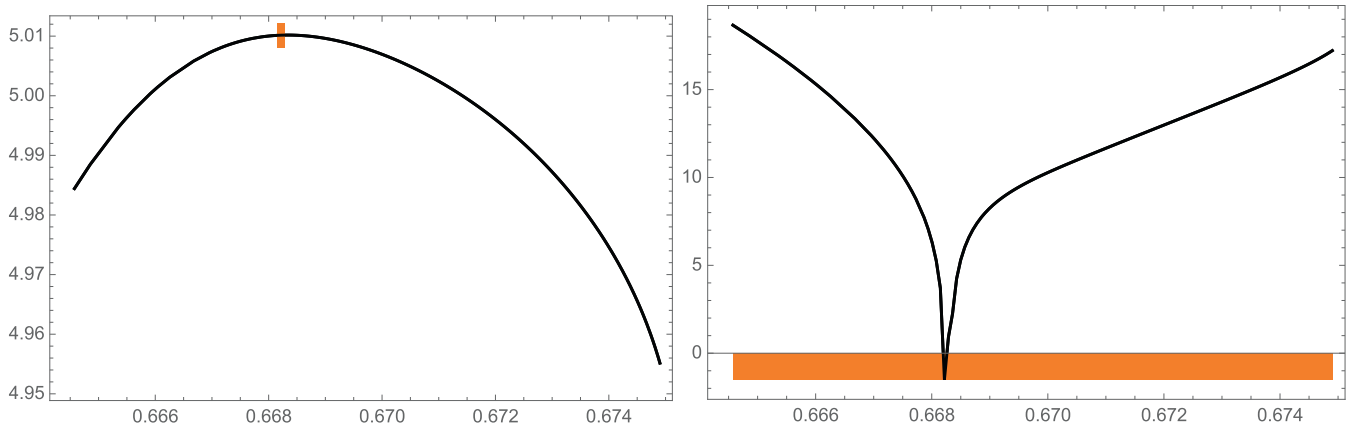

Fig. A.21. Family f_{21}.

References

Abad, A., Arribas, M., Palacios, M., Elipe, A., 2023. Evolution of the characteristic curves in the restricted three body problem in terms of the mass parameter. Celest. Mech. Dyn. Astron. 135, 7. https://doi.org/10.1007/s10569-022-10118-z.

Abad, A., Elipe, A., Ferreira, A.F.S., 2024. Periodic orbits around 216-Kleopatra asteroid modelled by a dipole-segment. Adv. Space Res. 74, 5687–5697. https://doi.org/10.1007/s10569-022-10118-z.

Bartczak, P., Breiter, S., 2003. Double material segment as the model of irregular bodies. Celest. Mech. Dyn. Astron. 86, 131–141. https://doi.org/10.1023/A:1024115015470.

Bartczak, P., Breiter, S., Jusiel, P., 2006. Ellipsoids, material points and material segments. Celest. Mech. Dyn. Astron. 96, 31–48. https://doi.org/10.1007/s10569-006-9017-x.

Broucke, R.A., Elipe, A., 2005. The dynamics of orbits in a potential field of a solid circular ring. Reg. Chaotic Dynam. 10, 129–143. https://doi.org/10.1070/RD2005v010n02ABEH000307.

Descamps, P., Marchis, F., Berthier, J., et al., 2011. Triplicity and physical characteristics of Asteroid 216-Kleopatra. Icarus 211, 1022–1033. https://doi.org/10.1016/j.icarus.2010.11.016.

Elipe, A., 2024. Wrong hypotheses in the generalized RTBP. Astophys. Space Sci. 369, 22. https://doi.org/10.1007/s10509-024-04286-7.

Elipe, A., Abad, A., Arribas, M., et al., 2021. Symmetric periodic orbits in the dipole-segment problem for two equal masses. Astron. J. 161, 274. https://doi.org/10.3847/1538-3881/abf353.

Elipe, A., Abad, A., & Ferreira, A.F.S. (2021). Dynamics of the Dipole-Segment with Equal Masses and Arbitrary Rotation, in Recent Trends in Chaotic, Nonlinear and Complex Dynamics, pp. 79–98 (2021) Chapter 4, World Sc. Ser. in Nonlinear Science Series B. pp. 79–98. doi: 10.1142/9789811221903_0004.

Elipe, A., Arribas, M., Kalvouridis, T.J., 2007. Periodic solutions in the planar (n + 1) ring problem with oblateness. J. Guid. Control Dynam. 30, 1640–1648. https://doi.org/10.2514/1.29524.

Elipe, A., da Costa, M.L., Piccotti, L., Tresaco, E., 2024. Close binary stars modelled by two prolate ellipsoids in synchronous rotation. AJ 167, 25, ttps://doi.org/10.3847/1538-3881/ad10a1.

Elipe, A., Riaguas, A., 2003. Nonlinear stability under a logarithmic gravity field. Int. Math. J. 3, 435–453.

Fujiwara, A., Kawaguchi, J., Yeomans, D.K., et al., 2006. The rubble-pile asteroid Itokawa as observed by Hayabusa. Science 312, 1330–1334. https://doi.org/10.1126/science.1125841.

Gómez, G., Llibre, J., Masdemont, J., 1988. Homoclinic and heteroclinic solutions in the restricted three-body problem. Celest. Mech. 44 (3), 239–259. https://doi.org/10.1007/BF01235538.

Gutiérrez, J.D., Tresaco, E., Riaguas, A., 2024. Analysis in the gravitations potential of elongated asteroids. Astrophys. Space Sci. 369, 67. https://doi.org/10.1007/s10509-024-04329-z.

Hénon, M., 1965. Exploration numérique du problème restreint. I Masses égales, Orbites periodiques, Annales d'Astrophysique 28, 499–511. BibCode: 1965AnAp...28.499H.

Hénon, M., 1997. Generating Families in the Restricted Three-Body Problem. Springer, ISBN: 3-540-63802-4.

Henrard, J., 1973. Proof of a conjecture of E. Strömgren. Celest. Mech. 7. https://doi.org/10.1007/BF01227510, 499-457.

Hirabayashi, M., Scheeres, D.J., 2014. Analysis of asteroid 216-Kleopatra using dynamical and structural constraints. Ap. J. 780, 160. https://doi.org/10.1023/A:1008233828923.

Markellos, V.V., Black, W., Moran, P.E., 1974. A grid search for families of periodic orbits in the restricted problem of three todies. Celest. Mech. 9, 507–512. https://doi.org/10.1007/BF01329331.

Ostro, S.J. et al., 2004. Extreme elongation of asteroid 1620 Geographos from radar images. Nature 375, 474–477. https://doi.org/10.1038/375474a0.

Palacios, M., Arribas, M., Abad, A., Elipe, A., 2019. Symmetric periodic orbits in the Moulton-Copenhagen problem. Celest. Mech. Dyn. Astron. 131, 16. https://doi.org/10.1007/s10569-019-9893-5.

Prieto-Llanos, T., Gómez-Tierno, M.A., 1994. Stationkeeping at libration points of natural elongated bodies. J. Guid. Control Dynam. 17, 787–794. https://doi.org/10.2514/3.21268.

Riaguas, A., 1999. Dinámica orbital alrededor de cuerpos celestes con forma irregular Ph.D. dissertation. Universidad de Zaragoza, Spain (in Spanish).

Riaguas, A., Elipe, A., López-Moratalla, T., 2001. Nonlinear stability of the equilibria in the gravity field of a finite straight segment. Celest. Mech. Dyn. Astron. 81, 235–248. https://doi.org/10.1023/A:1013217913585.

Strömgren, E., 1933. Connaissance actuelle des orbites dans le problème des trois corps. Bull. Astron. 9, 87–130, ibCode: 1933BuAst...9...87S.

Szebehely, V., 1967. Theory of Orbits. The Restricted Problem of Three Bodies. Academic Press, New York.

Werner, R.A., 1994. The gravitational potential of a homogeneous polyhedron or don't cut corners. Celest. Mech. Dyn. Astron. 59, 253–278. https://doi.org/10.1007/BF00692875.

Werner, R.A., Scheeres, D.J., 1997. Exterior gravitation of a polyhedron derived and compared with harmonic and mascon gravitation representations of Asteroid 4769 Castalia. Celest. Mech. Dyn. Astron. 65, 313–344. https://doi.org/10.1007/BF00053511.

Zeng, X., Liu, X., 2017. Searching for time optimal periodic orbits near irregularly shaped asteroids by using an indirect method. IEEE Trans. Aerosp. Electron. Syst. 53, 1221–1229. https://doi.org/10.1109/TAES.2017.2668071.

Zeng, X., Zhang, Y., Yu, Y., Liu, X., 2018. The dipole segment model for axisymmetrical elongated asteroids. AJ 155, 85. https://doi.org/10.3847/1538-3881/aaa483.

Zhang, Y., Zeng, X., Liu, X., 2018. Study on periodic orbits around the dipole segment model for dumbbell-shaped asteroids. Sci. China Technol. Sci. 61, 819–829. https://doi.org/10.1007/s11431-017-9099-y.